

## THE DIRECT DETECTABILITY OF GIANT EXOPLANETS IN THE OPTICAL

JOHNNY P. GRECO\* AND ADAM BURROWS†

Department of Astrophysical Sciences, Princeton University, Princeton, NJ 08544

*Draft version October 8, 2018*

### ABSTRACT

Motivated by the possibility that a coronagraph will be put on WFIRST/AFTA, we explore the direct detectability of extrasolar giant planets (EGPs) in the optical. We quantify a planet’s detectability by the fraction of its orbit for which it is in an observable configuration ( $f_{\text{obs}}$ ). Using a suite of Monte Carlo experiments, we study the dependence of  $f_{\text{obs}}$  upon the inner working angle (IWA) and minimum achievable contrast ( $C_{\text{min}}$ ) of the direct-imaging observatory; the planet’s phase function, geometric albedo, single-scattering albedo, radius, and distance from Earth; and the semi-major axis distribution of EGPs. We calculate phase functions for a given geometric or single-scattering albedo, assuming various scattering mechanisms. We find that the Lambertian phase function can predict significantly larger  $f_{\text{obs}}$ ’s with respect to the more realistic Rayleigh phase function. For observations made with WFIRST/AFTA’s baseline capabilities ( $C_{\text{min}} \sim 10^{-9}$ , IWA  $\sim 0.2''$ ), Jupiter-like planets orbiting stars within 10, 30, and 50 parsecs of Earth have volume-averaged observability fractions of  $\sim 12\%$ ,  $3\%$ , and  $0.5\%$ , respectively. At 10 parsecs, such observations yield  $f_{\text{obs}} > 1\%$  for low- to modest-eccentricity planets with semi-major axes in the range  $\sim 2 - 10$  AU. If  $C_{\text{min}} = 10^{-10}$ , this range extends to  $\sim 35$  AU. We find that, in all but the most optimistic configurations, the probability for detection in a blind search is low ( $< 5\%$ ). However, with orbital parameter constraints from long-term radial-velocity campaigns and *Gaia* astrometry, the tools we develop in this work can be used to determine both the most promising systems to target and when to observe them.

*Subject headings:* planetary systems – planets and satellites: general

### 1. INTRODUCTION

In the burgeoning field of exoplanetary science, the scientific return from direct imaging has so far been meager when compared to the very successful radial-velocity and transit methods. This delay in progress has been primarily due to the technological challenge of performing high-contrast observations at small angular separations (Oppenheimer & Hinkley 2009; Traub & Oppenheimer 2010). For a Jupiter twin, the planet/star flux ratio is expected to be  $\sim 10^{-7}$  in the mid-infrared and  $\sim 10^{-9}$  in the optical, and if the planet is in close proximity to Earth ( $< 30$  pc), these contrasts must be achieved at angular separations of a few tenths of arcseconds. Making the problem harder still, the direct detectability of a given planet will vary with time, depending upon its Keplerian orbital elements and atmospheric properties—which will depend upon the planet’s age, mass, orbital distance, and parent star (Sudarsky et al. 2005; Kane & Gelino 2010, 2011; Madhusudhan & Burrows 2012).

Despite these challenges, recent progress has been made via high-contrast observations in the near-infrared of nearby, young extrasolar giant planets (EGPs)/brown dwarfs at very wide orbital separations ( $\sim 10 - 200$  AU). Such substellar companions are self-luminous and provide contrasts and angular separations that are far more favorable than the case of a nearby Jupiter twin. Indeed, there have been a number of notable discoveries and partial characterizations, including 2MASS 1207b (Chauvin et al. 2004), AB Pic b (Chauvin et al. 2005), GQ Lup b (Neuhäuser et al. 2005),  $\beta$ -Pictoris b (La-

grange et al. 2009), HR 8799bcde (Marois et al. 2008, 2010; Barman et al. 2011), and GJ 504b (Kuzuhara et al. 2013). In the coming years, a plethora of high-contrast instruments such as the ground-based GPI (Macintosh et al. 2008), SPHERE (Beuzit et al. 2008), LBTI (Skrutskie et al. 2010), ScExAO/Charis/HICIAO (Suzuki et al. 2010) and the space-based NIRCcam and MIRI on JWST (Deming et al. 2009) will almost certainly produce a rich sample of directly imaged and characterized young EGPs (Beichman et al. 2010).

All of the above high-contrast imaging efforts are focused on measurements in the infrared. However, optical measurements of albedo spectra, phase curves, and polarization—which have been used to infer chemical compositions and cloud properties of several planets and moons in the solar system (Hansen & Hovenier 1974; Karkoschka 1994; Satoh et al. 2000; Irwin et al. 2002; Karkoschka & Tomasko 2011)—have enormous potential to constrain exoplanet atmospheric compositions, Keplerian elements, and aerosol and cloud properties (Marley et al. 1999; Sudarsky et al. 2000, 2003, 2005; Burrows et al. 2004; Seager et al. 2000; Stam et al. 2004; Dyudina et al. 2005; Buenzli & Schmid 2009; Cahoy et al. 2010; Madhusudhan & Burrows 2012; Burrows 2014; Marley et al. 2014). Additionally, optical reflected-light observations are sensitive to cool, mature EGPs at wide orbital distances, a population of planets that has been inaccessible to infrared measurements. Direct imaging and characterization of cool, mature EGPs will require a space-based high-contrast instrument such as the anticipated optical imaging and spectrophotometric coronagraph that is being designed for the Wide-Field Infrared Survey Telescope (WFIRST)/Astrophysics Focused Telescope Assets (AFTA) mission. If realized, this

\*jgreco@astro.princeton.edu

†burrows@astro.princeton.edu

instrument will achieve planet/star contrast ratios better than  $\sim 10^{-9}$  and an inner working angle near or better than  $\sim 0.2''$  (Spergel et al. 2015), well within the necessary capability to detect a Jupiter twin located  $\sim 20$  pc from Earth<sup>1</sup>. Therefore, studies of the observational signatures and direct detectability of reflected light from EGPs are particularly timely and will aid in the design and optimization of WFIRST/AFTA or a similar space-based effort.

In this work, we present an exploration of the direct detectability of cool EGPs at visible wavelengths ( $\sim 0.4\text{--}1.0\ \mu\text{m}$ ). We quantify a planet’s direct detectability by the fraction of its orbit for which it is in an observable configuration (its observability fraction  $f_{\text{obs}}$ ). Using a suite of Monte Carlo (MC) experiments, we explore the dependence of  $f_{\text{obs}}$  upon various input parameters such as the inner working angle (IWA), minimum achievable contrast ( $C_{\text{min}}$ ), planetary albedo and radius, distance from Earth, and the semi-major axis distribution of EGPs. We assume cloud-free, homogeneous atmospheres and calculate phase functions for a given geometric or single-scattering albedo, assuming different scattering mechanisms. Although partly motivated by the possibility of an optical coronagraph on WFIRST/AFTA, our study is relevant to any effort to directly detect exoplanets in the optical.

In §2 we describe how we model reflected-light observations of EGPs. We tabulate and provide analytic fits to the geometric albedo as a function of single-scattering albedo for scalar and vector Rayleigh, Lambert, and isotropic scattering. In addition, we present representative albedo spectra for homogeneous atmospheres of cool EGPs. This section is supported by an appendix, which reviews the equations that connect the Keplerian orbital elements to the observed phase angle and time. In §3 we present illustrative calculations of the variation of planet/star flux ratios and angular separations with orbital parameters, which ultimately determines an exoplanet’s direct detectability. In §4 we describe our MC experiments and discuss the assumptions we make about the orbital parameter distributions of EGPs.

Our results are given in §5. In §5.1 we present a parametric study of the mean observability fraction,  $\langle f_{\text{obs}} \rangle$ , for many MC experiments, which are run under different sets of assumptions. In §5.2 we highlight the fact that  $\langle f_{\text{obs}} \rangle$  for a population of planets is proportional to the probability that a blind search for such planets will yield a detection. Equivalently,  $\langle f_{\text{obs}} \rangle$  can be interpreted as the probability for detection, assuming all stars have one such planet. In §5.3 we briefly consider the optical signature of thermal emission from young EGPs. The paper is brought to close in §6 with a summary of our results.

Throughout this paper, we define a “Jupiter-like” planet to be an EGP with the radius of Jupiter, a geometric albedo of 0.5, and a Rayleigh scattering atmosphere. Although these atmospheric properties are not consistent with Jupiter at all wavelengths, near  $\sim 0.565\ \mu\text{m}$ , which is at the center of one of the WFIRST/AFTA bandpasses, they provide a decent approximation to observations (Karkoschka 1994).

<sup>1</sup> For a summary of the diagnostic potential for cold exoplanet characterization using the anticipated WFIRST/AFTA coronagraph, see Burrows (2014), Marley et al. (2014), and Hu (2014).

## 2. MODELING REFLECTED-LIGHT OBSERVATIONS OF GIANT EXOPLANETS

To directly detect an extrasolar planet, its dim light must be separated from the overwhelming glare of its bright parent star. For a given high-contrast imaging observation, this requires that two conditions be *simultaneously* satisfied: 1) the planet/star contrast ratio ( $F_p/F_\star$ ) must be above the minimum achievable contrast ( $C_{\text{min}}$ ), and 2) the planet/star angular separation ( $\delta\phi$ ) must be both larger than the inner working angle (IWA) and smaller than the outer working angle (OWA). As a further complication,  $C_{\text{min}}$  will typically be a function of  $\delta\phi$ , and both of these parameters will depend upon the wavelength of the observation. Thus, the direct detectability of an exoplanet ultimately depends upon its location in  $(F_p/F_\star) - \delta\phi$  parameter space, which is a complicated function of time, orbital and atmospheric parameters, and the high-contrast imaging technology used to make the observation. In this section, we describe the methods we employ to predict the direct detectability of EGPs as they move through  $(F_p/F_\star) - \delta\phi$  parameter space.

### 2.1. Planet/Star Contrast Ratios: Albedos and Phase Functions

At optical wavelengths ( $\sim 0.4\text{--}1.0\ \mu\text{m}$ ), the flux from a giant exoplanet is dominated by reflected starlight, provided the planet is sufficiently old and of low enough mass that its thermal emission is negligible (see §5.3 for a discussion of thermal emission from young EGPs). Observationally, the wavelength- and phase-dependence of this reflection is encompassed by the geometric albedo spectrum,  $A_g(\lambda)$ , and the classical phase function,  $\Phi(\lambda, \alpha)$ . Here,  $\lambda$  is the photon wavelength, and  $\alpha$  is the exoplanet-centric angle between the star and the observer. In terms of these parameters, the planet/star flux ratio is given by

$$\frac{F_p}{F_\star} = A_g(\lambda) \left( \frac{R_p}{d} \right)^2 \Phi(\lambda, \alpha), \quad (1)$$

where  $R_p$  is the planet radius and  $d$  is the orbital distance (see appendix, Equation (A.2)).  $\Phi(\alpha, \lambda)$  is normalized to unity at full phase ( $\alpha = 0^\circ$ ), which defines the geometric albedo. The planet’s atmospheric composition, temperature/pressure structure, cloud/haze profiles, and scattering properties govern  $A_g(\lambda)$  and  $\Phi(\lambda, \alpha)$ . Hence, observations of optical planet/star flux ratios, as a function of wavelength and phase angle, have great potential to constrain the theory of exoplanet atmospheres (e.g., Marley et al. 1999; Sudarsky et al. 2000; Burrows et al. 2004; Cahoy et al. 2010). Furthermore, the shape and magnitude of an exoplanet’s phase-folded light curve are highly sensitive to the Keplerian elements of its orbit (Sudarsky et al. 2005; Dyudina et al. 2005; Kane & Gelino 2010, 2011; Madhusudhan & Burrows 2012), providing an independent method for measuring orbital parameters that complements astrometric and radial-velocity methods.

In this work, we are interested in the general character, as opposed to detailed quantitative predictions, of the direct detectability of EGPs. We, therefore, generally assume planets with constant  $A_g$  (the exception is in §5.1.5, where we vary  $A_g$  with orbital distance using two simple models) and use the formalism presented in Madhusudhan & Burrows (2012) to calculate the associated single-scattering albedo ( $\omega$ ) and phase function for an as-

**Table 1**  
Geometric albedos as a function of single-scattering albedo

$\omega$	$A_g$			
	Lambert	Isotropic	Scalar Rayleigh	Vector Rayleigh
0.005	0.0033334	0.00062685	0.0009394	0.00094
0.01	0.0066668	0.0012574	0.0018826	0.00188
0.05	0.033334	0.0064412	0.0095705	0.00963
0.1	0.066668	0.013293	0.01956	0.0198
0.15	0.1	0.020604	0.030015	0.03057
0.2	0.13334	0.028429	0.040992	0.04201
0.25	0.16667	0.036836	0.052557	0.0542
0.3	0.2	0.045906	0.064788	0.06723
0.35	0.23334	0.055736	0.077783	0.08121
0.4	0.26667	0.066447	0.09166	0.09628
0.45	0.3	0.078189	0.10657	0.11261
0.5	0.33334	0.091154	0.12269	0.13041
0.55	0.36667	0.10559	0.14029	0.14996
0.6	0.40001	0.12183	0.15968	0.17161
0.65	0.43334	0.14033	0.18131	0.19585
0.7	0.46667	0.16174	0.20583	0.22336
0.75	0.50001	0.18703	0.2342	0.25514
0.8	0.53334	0.21777	0.26799	0.29281
0.85	0.56668	0.25672	0.30994	0.33916
0.9	0.60001	0.30957	0.36572	0.39991
0.95	0.63334	0.392	0.45097	0.49069
0.99	0.66001	0.53463	0.59585	0.64034
0.999	0.66601	0.63582	0.69783	0.74337
1.0	0.66668	0.68956	0.75165	0.79766

**Note.** — These calculations were carried out with the formalism described in Madhusudhan & Burrows (2012).

summed scattering mechanism. In Table 1, we have tabulated  $A_g$  as a function of  $\omega$  for scalar and vector Rayleigh scattering, Lambert reflection, and isotropic scattering. Unless stated otherwise, we will hereafter refer to vector Rayleigh scattering as Rayleigh scattering.

The geometric albedo for a Lambert surface has a well-known analytic expression:  $A_g(\omega) = (2/3)\omega$ . Analytic fits to  $A_g(\omega)$  for isotropic (iso) and scalar/vector (sca/vec) Rayleigh scattering are:

$$A_g^{\text{iso}} = 0.6896 \frac{(1 + 0.4380s)(1 - s)}{(1 + 1.2966s)(1 + 0.7269s)}, \quad (2)$$

$$A_g^{\text{sca}} = 0.8190 \frac{(1 + 0.1924s)(1 - s)}{(1 + 1.5946s)(1 + 0.0886\omega)}, \quad (3)$$

$$A_g^{\text{vec}} = 0.6901 \frac{(1 + 0.4664s)(1 - s)}{(1 + 1.7095s)(1 - 0.1345\omega)}, \quad (4)$$

where  $s \equiv \sqrt{1 - \omega}$ . These fits are accurate to within 0.5% for all  $\omega$ , with the largest discrepancies corresponding to  $\omega < 0.4$ <sup>2</sup>. Fits such as these are particularly useful for efficient theoretical calculations of the geometric albedo, as well as for retrieving a representative atmosphere-averaged scattering albedo from an observed geometric albedo.

It is common to assume the Lambert phase function when modeling reflected-light observations. However, this assumption neglects the albedo- and wavelength-dependence of physical phase curves, and generally predicts higher values than the more physically motivated Rayleigh phase function (Madhusudhan & Burrows

<sup>2</sup> Madhusudhan & Burrows (2012) also provide an analytic fit to  $A_g^{\text{vec}}(\omega)$ , which is marginally better than Equation (4) for small  $\omega$ , but considerably less accurate for  $\omega$  close to unity.

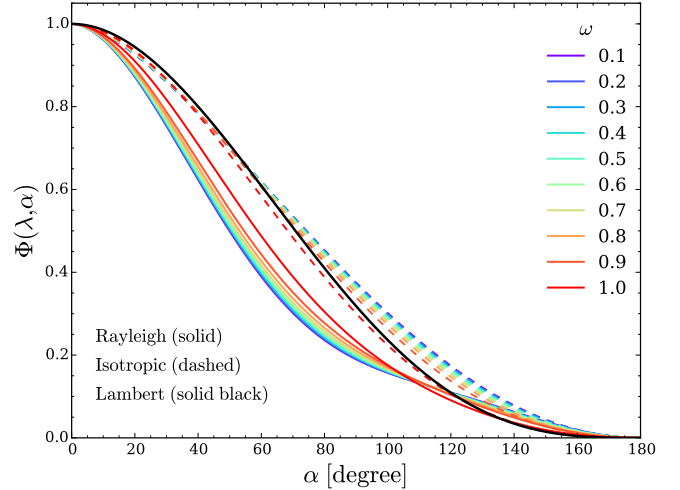


**Figure 1.** Comparison of phase functions for Rayleigh, isotropic, and Lambert scattering. The colors correspond to the indicated single-scattering albedos ( $\omega$ ). Note that the Lambert phase function (solid black line) is independent of  $\omega$ .

2012). Figure 1 compares the phase curves for scattering due to Rayleigh, isotropic, and Lambert scattering. We see that Rayleigh scattering phase curves are systematically lower than isotropic and Lambert phase curves for  $\alpha \lesssim 120^\circ$ , differing by as much as a factor of  $\sim 2$  for phase angles in the range  $60^\circ \lesssim \alpha \lesssim 90^\circ$  (see also, Madhusudhan & Burrows 2012). For most phase angles, increasing  $\omega$  results in better agreement between these scattering processes. Rayleigh phase curves generally increase with increasing  $\omega$ , whereas isotropic scattering phase curves show the opposite trend. In §5.1.1, we compare predictions of the direct detectability of EGPs with Rayleigh, isotropic, and Lambert phase functions.

### 2.1.1. Keplerian Elements

Once  $\Phi(\lambda, \alpha)$  is obtained for a particular planet, the *observed* phase curve depends on the Keplerian elements of its orbit<sup>3</sup>. These include the semi-major axis ( $a$ ), orbital inclination ( $i$ ), eccentricity ( $e$ ), argument of periastron ( $\omega_p$ ), time of periastron passage ( $t_p$ ), and longitude of the ascending node ( $\Omega$ ) (Sudarsky et al. 2005; Dyudina et al. 2005; Kane & Gelino 2011; Madhusudhan & Burrows 2012). For an assumed stellar mass, the period of the planet’s orbit ( $P$ ) can be calculated from  $a$ . Note  $\Omega$  is necessary when an absolute celestial frame is designated (e.g., when measuring the full Stokes polarization or cataloguing many different systems in the same solar-system frame). However, one can assume  $\Omega = 90^\circ$  or simply ignore this parameter when the system itself is allowed to provide a natural orientation (e.g., in exoplanet radial-velocity measurements). Throughout this work, we will assume  $\Omega = 90^\circ$ .

### 2.1.2. Albedo Spectra from Homogeneous Atmospheres

Semi-infinite homogeneous atmospheres are characterized by an average single-scattering albedo spectrum:  $\omega(\lambda) \equiv \kappa_s / (\kappa_s + \kappa_a)$ , where  $\kappa_s$  is the scattering opacity, and  $\kappa_a$  is the absorptive opacity. In this section,

<sup>3</sup> See the appendix for a review of the equations that connect the Keplerian orbital elements to the observed phase angle and time.

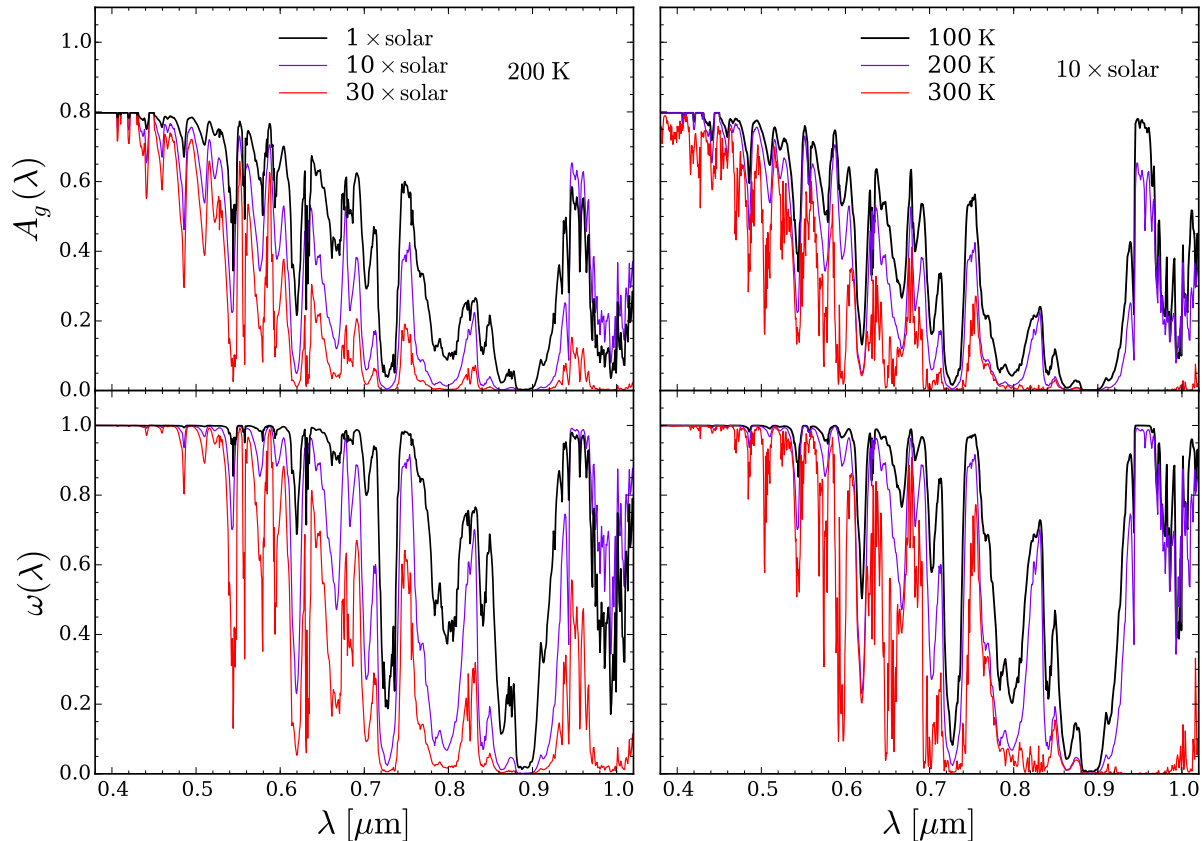


**Figure 2.** Demonstration of the strong dependence of geometric (top row) and scattering (bottom row) albedo spectra upon temperature and atmospheric metallicity. The models in the left column fix the temperature at  $T = 200\text{ K}$  and vary the metallicity, and those in the right column fix the metallicity at  $10 \times$  solar and vary the temperature. Note the methane features near  $\sim 0.62\ \mu\text{m}$ ,  $\sim 0.74\ \mu\text{m}$ ,  $\sim 0.81\ \mu\text{m}$ , and  $\sim 0.89\ \mu\text{m}$ , ammonia spectral bands near  $\sim 0.65\ \mu\text{m}$  and  $\sim 0.79\ \mu\text{m}$ , and broad water band at  $\sim 0.94\ \mu\text{m}$ . The models are cloud-free, homogeneous, semi-infinite, and use opacities at a pressure of 0.5 atmospheres. The calculations of  $\omega(\lambda)$  use the opacity database from Sharp & Burrows (2007) and the equilibrium chemical abundances from Burrows & Sharp (1999). The geometric albedo spectra assume purely Rayleigh scattering atmospheres.

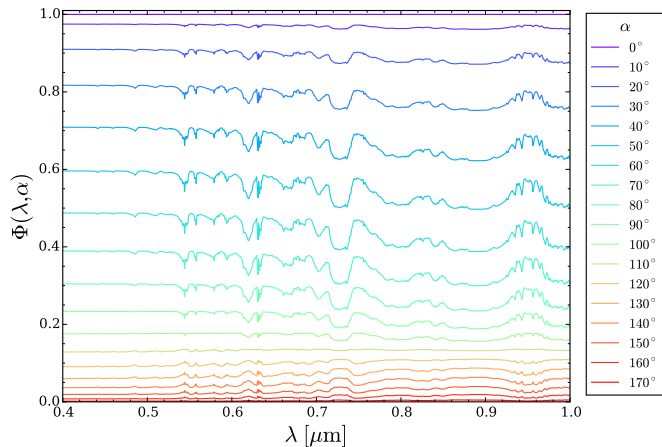


**Figure 3.** Example variation with wavelength and phase angle of the Rayleigh phase function, where we have assumed the single-scattering albedo spectrum (shown as the black line in the bottom left panel of Figure 2) of a semi-infinite homogeneous atmosphere with  $T = 200\text{ K}$ , solar metallicity, and a pressure of 0.5 atmospheres. For a Lambert surface, the phase curve does not depend upon wavelength, and the horizontal lines corresponding to each phase would be flat and featureless, while of course the corresponding geometric albedos retain a stiff dependence upon wavelength.

we provide illustrative scattering albedo spectra for cool

EGPs, which will aid in the interpretation of some of the results presented in this paper. Our calculations use the opacity database from Sharp & Burrows (2007) and the equilibrium chemical abundances from Burrows & Sharp (1999).

From its definition, it is clear that  $\omega(\lambda)$  is a function of atmospheric parameters such as temperature, pressure, and composition. In Figure 2, we demonstrate the characteristic strong dependence of scattering albedos (bottom row) and the corresponding Rayleigh scattering geometric albedos (top row) upon temperature and metallicity. The models are cloud-free, homogeneous, semi-infinite, and use opacities at a pressure of 0.5 atmospheres. For the temperatures and pressures relevant to cool EGPs, we find  $\omega(\lambda)$  is relatively insensitive to variations in atmospheric pressure. In general, higher temperatures/metallicities result in lower albedos, particularly for wavelengths longward of  $\sim 0.65\ \mu\text{m}$ .

The spectra in Figure 2 show prominent methane features near  $\sim 0.62\ \mu\text{m}$ ,  $\sim 0.74\ \mu\text{m}$ ,  $\sim 0.81\ \mu\text{m}$ , and  $\sim 0.89\ \mu\text{m}$ , ammonia spectral bands near  $\sim 0.65\ \mu\text{m}$  and  $\sim 0.79\ \mu\text{m}$ , and a broad water band at  $\sim 0.94\ \mu\text{m}$ . Although there is clearly some degeneracy between metallicity and temperature, this figure suggests optical flux ratio measurements, particularly between  $\sim 0.5 - 0.6\ \mu\text{m}$  and/or  $\sim 0.82\ \mu\text{m}$  and  $\sim 0.94\ \mu\text{m}$ , have great potential as temperature/composition diagnostics.

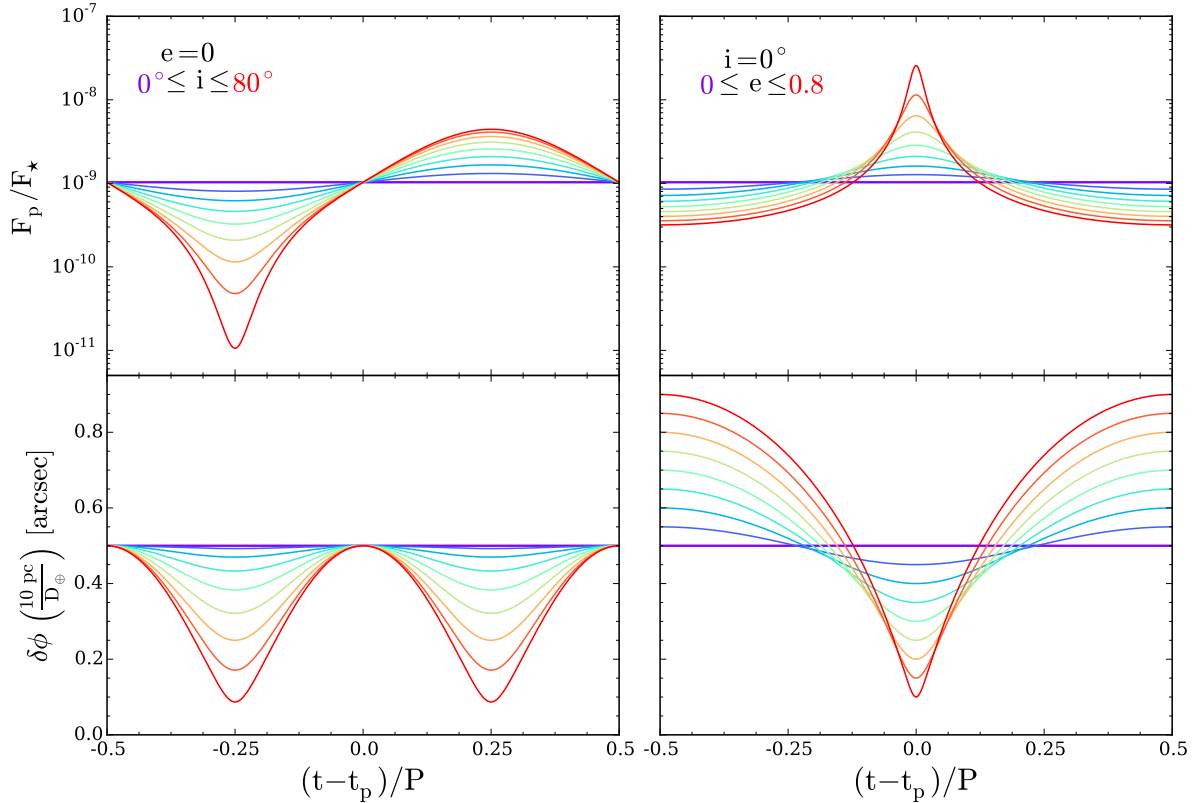


**Figure 4.** The top row shows the time dependence of the planet/star flux ratio for circular orbits with many different inclinations (left) and face-on orbits with many different eccentricities (right). The bottom row shows the corresponding planet/star angular separation, assuming the system is located 10 pc from Earth. All calculations assume a Jupiter-like planet in an orbit with  $a = 5$  AU and  $\omega_p = 0^\circ$ .

Given a single-scattering albedo spectrum, one can use the formalism presented in Madhusudhan & Burrows (2012) to calculate the phase function for an assumed scattering process as a function of phase angle and wavelength. Note that the often-assumed Lambert phase function is independent of  $\omega(\lambda)$ , and hence  $\lambda$ . In Figure 3, we show the phase function for Rayleigh scattering as a function of wavelength and phase angle, where we have assumed the scattering albedo spectrum shown as the black line in the bottom left panel of Figure 2. As expected, the phase curve is equal to one for all  $\lambda$  at  $\alpha = 0^\circ$ , but note the variation in  $\Phi(\lambda, \alpha)$  as  $\alpha$  increases from  $0^\circ$  to  $170^\circ$ . In contrast, a Lambert surface would result in featureless, horizontal lines for all  $\alpha$ .

## 2.2. Planet/Star Angular Separation

In addition to the planet/star contrast ratio, the planet/star angular separation is an essential parameter in determining the feasibility of the direct detection of reflected light from an exoplanet. For coronagraphic observations, the figure of merit is given as an IWA and OWA. An IWA (OWA) is the minimum (maximum) planet/star angular separation that can be resolved by a given instrument. Using the formalism outlined in the appendix, the projected angular separation, as a function of phase angle and time, can be obtained via the following equation:

$$\delta\phi = \frac{d}{D_\oplus} \sqrt{\cos^2(\theta + \omega_p) + \sin^2(\theta + \omega_p) \cos^2 i}, \quad (5)$$

where  $D_\oplus$  is the system's distance from Earth and  $\theta$  is the planet's orbital angle as measured from periastron (the true anomaly). Inspection of the above equation reveals that, as with the planet/star flux ratio, the time dependence of the planet/star angular separation will depend sensitively upon the Keplerian orbital elements.

## 3. VARIATION OF FLUX RATIOS AND ANGULAR SEPARATIONS WITH ORBITAL PARAMETERS

Using the methods presented in §2 to calculate planet/star flux ratios and angular separations, we now present example realizations of the  $(F_p/F_*) - \delta\phi$  parameter space for EGPs. The calculations in this section are representative of those that will be used in our Monte Carlo experiments, which are presented in §4. Several previous studies have also investigated this parameter space. In particular, Kane & Gelino (2010, 2011) considered the eccentricity and inclination dependence of exoplanet phase signatures, Kane (2013) used the eccentricity distribution of known exoplanets to study the completeness of imaging surveys, and Janson (2010) studied the effect that prior knowledge of orbital inclination has on the efficiency of directly imaging Earth-like planets. In this paper, we build on previous work by performing a systematic study of the dependence of the direct detectability of EGPs upon a wide range of technological and astrophysical parameters (§5).

### 3.1. Eccentricity and Inclination

As mentioned in §2.1.1 and §2.2, observed flux ratios and separations are strong functions of the Keplerian or-



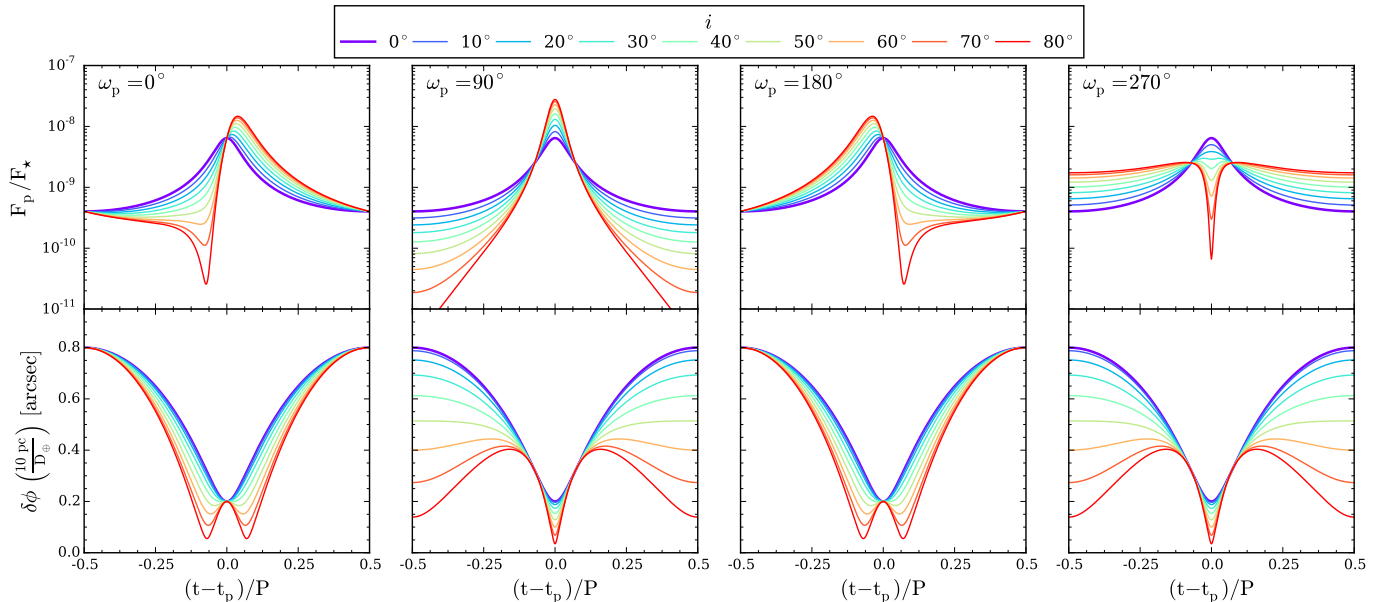


**Figure 5.** Planet/star flux ratios (top row) and angular separations (bottom row) for a Jupiter-like planet at a distance  $D_{\oplus} = 10$  pc from Earth on an orbit with  $e = 0.6$  and  $a = 5$  AU. Each column corresponds to orbits with the periastron argument indicated in each top left corner, and the colors represent the indicated inclinations. For the orbit orientation, we use the convention  $\alpha = \theta = 0^\circ$  when  $\omega_p = i = 90^\circ$ , implying full phase corresponds to the time of periastron passage when  $\omega_p = 90^\circ$ . Note that the detectability of planets on face-on orbits (purple lines) is independent of  $\omega_p$ .

bitual elements. Figure 4 demonstrates this dependence for circular orbits with many different inclinations (left column) and face-on orbits with many different eccentricities (right column). The top row shows planet/star flux ratios, and the bottom row shows the corresponding angular separations for a system located 10 pc from Earth. All calculations in this figure assume a Jupiter-like planet in an orbit with  $a = 5$  AU and  $\omega_p = 0^\circ$ .

Although it has been pointed out previously in the literature, it is worth reemphasizing that direct-imaging observations are well-suited for studying face-on systems (the opposite is true for the radial-velocity and transit methods, which are biased towards high-inclination systems). The reason for this is that an exoplanet on a circular, face-on orbit with  $F_p/F_\star > C_{\min}$  and  $\delta\phi > \text{IWA}$  will be directly detectable at all times (note we are assuming  $\delta\phi < \text{OWA}$ ). If, on the other hand, its inclination is  $\sim 90^\circ$ , both the planet/star flux ratio and angular separation will drop below their detection thresholds for some fraction of the orbit as the planet passes through the full range of possible phase angles. For instance, if  $C_{\min} = 10^{-10}$  and  $\text{IWA} = 0.3''$ , then a face-on orbit (flat purple lines in Figure 4) will be well above the detection thresholds at all times. However, as we increase the inclination in the left column of this figure, we see that the flux ratio dips below  $C_{\min}$  for an increasingly larger fraction of the orbit centered at new phase ( $\alpha = 180^\circ$ ). Similarly, the minimum planet/star angular separation decreases with increasing inclination, falling below the IWA for an increasingly larger fraction of the orbit centered at new phase *and* full phase. Although the flux ratio near full phase is largest for high-inclination orbits, the planet will still be undetectable due to the small planet/star angular separation.

In the right column of Figure 4, we show the effect of increasing the eccentricity of a face-on orbit from circular ( $e = 0$ ) to highly eccentric ( $e = 0.8$ ). In this case,

the phase variations are due to the time dependence of the orbital distance. On one hand, a planet on a highly eccentric orbit can be an excellent direct-imaging target, as it spends a large fraction of its orbit at larger orbital distances from its parent star, and for certain sets of Keplerian elements, this can provide angular separations that are highly favorable for direct-imaging observations. This, however, comes at the cost of lower flux ratios throughout most of its orbit and very small angular separations when it is near periastron passage.

### 3.2. Argument of Periastron and Inclination

As has been pointed out by Kane & Gelino (2011), the interaction between the argument of periastron and inclination in  $(F_p/F_\star) - \delta\phi$  parameter space can be quite complex. Figure 5 shows various combinations of these parameters for a Jupiter-like planet on an eccentric orbit with  $e = 0.6$  and  $a = 5$  AU. Each column shows planet/star flux ratios and angular separations for orbits with inclinations that vary from  $0^\circ$  to  $80^\circ$ , with the argument of periastron held constant at the value indicated in each top left corner. Note we use the convention that when  $\alpha = \theta = 0^\circ$ ,  $\omega_p = i = 90^\circ$ . In other words, periastron passage coincides with full phase when the argument of periastron is  $90^\circ$  and with new phase when it is  $270^\circ$ .

The detectability of planets on face-on orbits is independent of  $\omega_p$ , as can be seen by the constant purple curve in all panels of Figure 5. As we increase the inclination, the flux ratio can either increase or decrease, depending upon the periastron argument and phase of the orbit. For  $\omega_p = 90^\circ$ , the flux ratio decreases with inclination for most of the orbit as the planet transitions from being permanently oriented at quarter phase when  $i = 0^\circ$  to displaying nearly all phase angles when  $i = 80^\circ$ . At full phase, which corresponds to periastron passage, the flux ratio achieves its maximum for this set of parameters. However, as is typically the case, this maxi-

imum flux ratio corresponds to a minimum planet/star angular separation that, in the limit of a perfectly edge-on system, drops to zero at the time of periastron passage. Interesting behavior also occurs when  $\omega_p = 270^\circ$ . For this periastron argument, periastron passage corresponds to new phase, and, in exactly the opposite sense from the  $\omega_p = 90^\circ$  case, the flux ratio increases with inclination for most of the orbit and results in a minimum at the time of periastron passage for high-inclination orbits. For orbits with  $i \gtrsim 50^\circ$ , the minimum angular separation actually coincides with the minimum flux ratio, and the maximum angular separation coincides with the relatively large fraction of the orbit with a large flux ratio.

#### 4. MONTE CARLO EXPERIMENTS

We have performed a set of Monte Carlo (MC) experiments, in which we generate random orbits and calculate the fraction of time a giant planet on each orbit would be directly detectable in the optical. We define this fraction to be the observability fraction,  $f_{\text{obs}}$ , and we calculate its value under many different assumptions. An illustrative calculation of  $f_{\text{obs}}$  for a Jupiter-like planet on a random orbit around a star located 10 pc from Earth is shown in Figure 6. We have assumed a direct-imaging observatory with  $C_{\text{min}} = 10^{-9}$  and IWA =  $0.2''$ , which are the baseline coronagraph design parameters for WFIRST/AFTA. The purple curve represents the planet/star contrast ratio (left axis), the red curve shows the corresponding angular separation (right axis), and the corresponding detection thresholds are indicated by the dashed lines. For the planet to be detectable, each curve must be above its associated dashed line. This is true only for times within the gray hatched region. A Jupiter-like planet on this particular orbit would have  $f_{\text{obs}} \approx 20\%$ . Given an estimate of the occurrence rate of such planets, the mean  $f_{\text{obs}}$  for many systems can be translated into the probability that a direct-imaging observation of a random star will result in a detection (see §5.2).

##### 4.1. Orbital Parameter Distributions

Each random orbit requires the generation of four Keplerian elements:  $\{a, e, i, \omega_p\}$ . To accomplish this, we assume planetary orbital orientations are isotropically distributed with respect to the observer, which leads to periastron arguments distributed uniformly in  $[0, 2\pi]$  and  $\cos i$  distributed uniformly in  $[-1, 1]$ . The semi-major axis and eccentricity distributions must be determined empirically. Most of our knowledge of these distributions has come from radial-velocity (Cumming et al. 2008; Howard et al. 2010) and transit (Batalha et al. 2013; Fressin et al. 2013) surveys that are biased towards short-period planets and have only been in operation long enough to fully describe planets with periods up to a few thousand days.

Nevertheless, we assume both the semi-major axis and eccentricity distributions derived from radial-velocity planets can be extrapolated to wider separations. For the semi-major axis distribution, we adopt a power-law,  $dN/da \propto a^\beta$ , where our fiducial calculations assume  $\beta = -0.61$  (Cumming et al. 2008). This distribution is based on radial-velocity planets with orbital periods in the range 2 – 2000 days, corresponding to semi-major

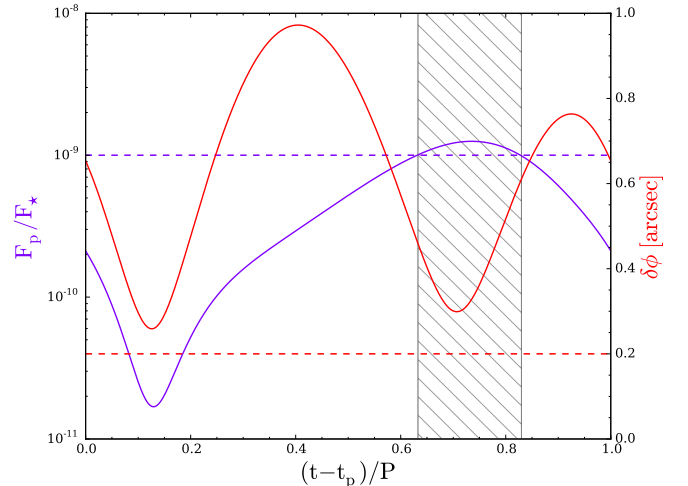


**Figure 6.** The planet/star flux ratio (purple, left axis) and angular separation (red, right axis) of a Jupiter-like planet orbiting a star 10 pc from Earth on a randomly generated orbit with  $\{a, e, i, \omega_p\} = \{8.7 \text{ AU}, 0.14, 71^\circ, 211^\circ\}$ . Assuming  $C_{\text{min}} = 10^{-9}$  and IWA =  $0.2''$ , which are indicated by the purple and red dashed lines, this planet would be directly detectable at times within the gray hatched region. The observability fraction of this planet is  $f_{\text{obs}} \approx 20\%$ .

axes in the range 0.03 – 3.0 AU. Results from direct-imaging surveys have been used to set model-dependent limits on the maximum semi-major axis ( $a_{\text{max}}$ ) to which the radial-velocity distribution can be extrapolated. Using Monte Carlo simulations to examine the null results from direct-imaging searches for EGPs around 118 stars, Nielsen & Close (2010) determined  $a_{\text{max}} \sim 65 - 234 \text{ AU}$ , depending on the assumed planet luminosity model. Brandt et al. (2014) performed a statistical analysis of direct-imaging data from a sample of nearly 250 stars, finding  $a_{\text{max}} \sim 30 - 100 \text{ AU}$ , which again depends on the adopted cooling model. With these studies as our motivation, our fiducial calculations assume the semi-major axis distribution is given by a power-law with a minimum  $a_{\text{min}} = 0.03 \text{ AU}$  and a maximum  $a_{\text{max}} = 65 \text{ AU}$ .

For the eccentricity distribution, we use the two-parameter Beta distribution given by Kipping (2013):

$$P_\beta(e; a, b) = \frac{\Gamma(a+b)}{\Gamma(a)\Gamma(b)} e^{a-1} (1-e)^{b-1}, \quad (6)$$

where  $\Gamma$  is the Gamma function. Our fiducial calculations assume  $a = 1.12$  and  $b = 3.09$ , which are the long-period parameters given by Kipping (2013), who derived this distribution by regressing the known cumulative density function of orbital eccentricities from exoplanets detected from the radial-velocity method. The orbits of planets with  $a < 0.1 \text{ AU}$  are expected to be rapidly circularized due to strong tidal forces. Although we do not expect the eccentricities of such planets to influence our results, we set  $e = 0$  for any planet with  $a < 0.1 \text{ AU}$ .

We find the direct detectability of EGPs is highly sensitive to the assumed semi-major axis distribution, but relatively insensitive to the eccentricity distribution. Our fiducial orbital parameter distributions are summarized in Table 2.

## 5. RESULTS

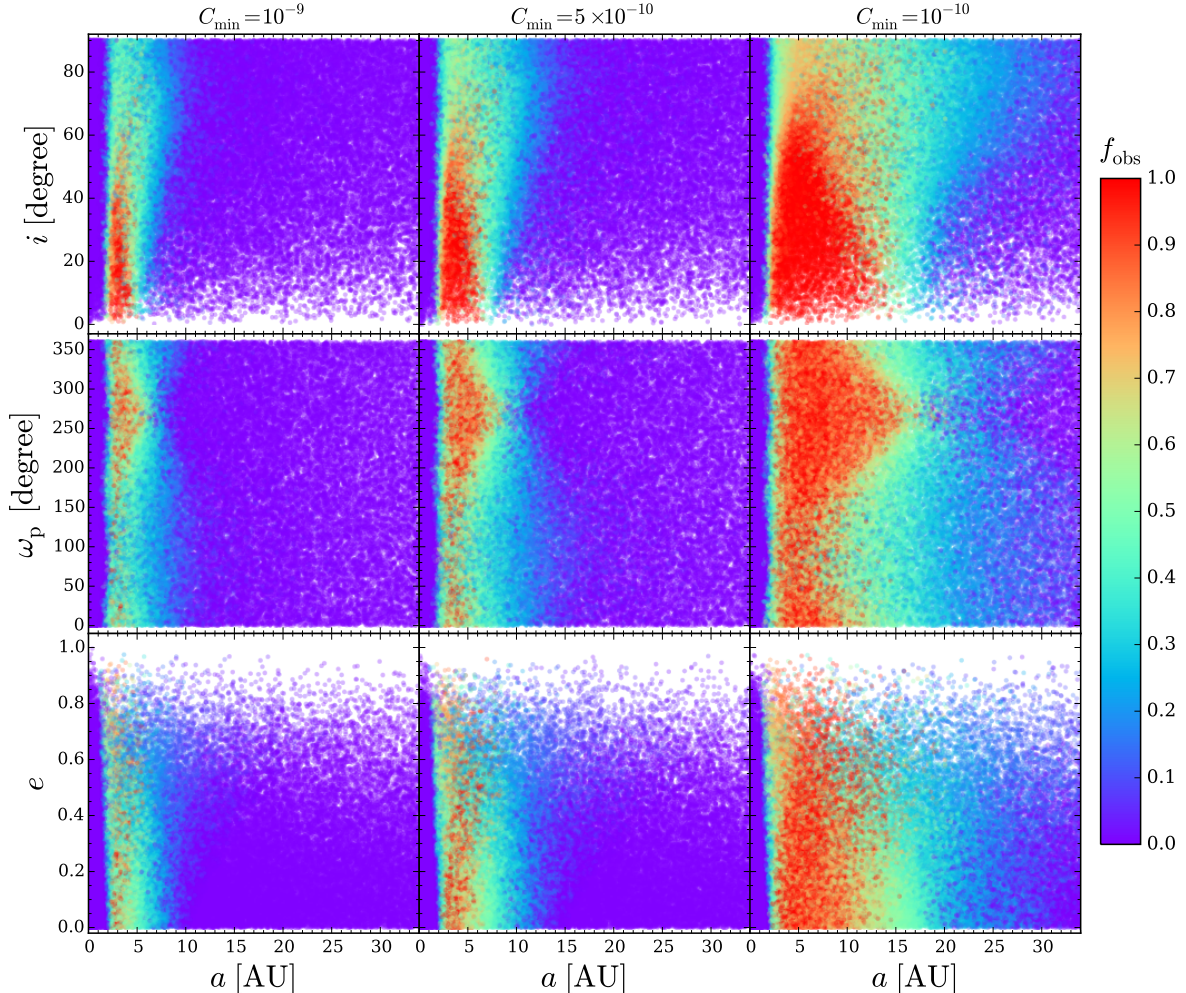


**Figure 7.** Distribution of observability fractions ( $f_{\text{obs}}$ ) as a function of orbital parameters for three illustrative MC experiments, where we have assumed  $C_{\text{min}} = 10^{-9}$  (left column),  $C_{\text{min}} = 5 \times 10^{-10}$  (middle column), and  $C_{\text{min}} = 10^{-10}$  (right column). Each experiment is composed of  $5 \times 10^5$  random orbits generated from the distributions given in Table 2. In each panel, dots indicate a single orbit, and the color-scale represents  $f_{\text{obs}}$ , which we calculate for direct observations of a Jupiter-like planet orbiting a star at a distance of  $D_{\oplus} = 10$  pc from Earth, using an instrument with IWA =  $0.2''$ , OWA =  $1.75''$ , and the minimum contrast indicated at the top of each column.

**Table 2**  
Fiducial Orbital Parameter Distributions

Parameter	Range	Distribution
$a$	[0.03 AU, 65 AU]	$dN/da \propto a^{\beta}$
$e$	[0, 1)	$P_{\beta}(e; a, b)^a$
$\cos i$	[-1, 1]	uniform
$\omega_p$	[0, $2\pi$ ]	uniform

**Note.** — For our fiducial semi-major axis distribution, we assume a power-law index  $\beta = -0.61$  (Cumming et al. 2008). For our fiducial eccentricity distribution, we assume  $a = 1.12$  and  $b = 3.09$ , which are the long-period parameters given in Kipping (2013). We set  $e = 0$  for any planet with  $a < 0.1$  AU.

<sup>a</sup>This is the Beta distribution from Kipping (2013) (Equation (6)).

### 5.1. Mean Observability Fractions

Here, we present a parametric study of the mean observability fraction,  $\langle f_{\text{obs}} \rangle$ , for different sets of MC experiments, each composed of  $5 \times 10^5$  random orbits. For a given population of planets,  $\langle f_{\text{obs}} \rangle$  can be interpreted as a detection probability, assuming all stars have one such

planet. In Figure 7, we show the distribution of  $f_{\text{obs}}$  as a function of orbital parameters for three illustrative MC experiments. Each column corresponds to an independent experiment, where we have assumed  $C_{\text{min}} = 10^{-9}$  (left column),  $C_{\text{min}} = 5 \times 10^{-10}$  (middle column), and  $C_{\text{min}} = 10^{-10}$  (right column). In all three cases, we use our fiducial orbital parameter distributions, and calculate  $f_{\text{obs}}$  for direct observations of a Jupiter-like planet orbiting a star at a distance of  $D_{\oplus} = 10$  pc from Earth, using an instrument with IWA =  $0.2''$ , OWA =  $1.75''$ , and the minimum contrast specified at the top of each column.

In a given panel, each dot represents a single orbit, and the color-scale shows the observability fraction for the indicated assumptions about the planet and direct-imaging observatory. For a fixed minimum contrast, the semi-major axis has by far the largest effect on  $f_{\text{obs}}$ , creating highly clustered regions of low and high values of  $f_{\text{obs}}$ . The sharp drop in observability interior to 2 AU corresponds to an angular separation of  $0.2''$ , which is the assumed IWA. Note, however, that eccentric orbits with  $a < 2$  AU are able to achieve nonzero observability



fractions, since a planet on such an orbit spends a large fraction of its time near orbital distances of  $a(1 + e)$ , making it possible for the observed angular separations to fall outside the IWA, provided the full set of Keplerian elements allows for such geometries. These results make it clear that  $f_{\text{obs}}$  is very sensitive to the assumed semi-major axis distribution. Steeper (shallower) power-law indices will result in narrower (broader) regions of high  $f_{\text{obs}}$  values, and the assumed values of  $a_{\text{max}}$  and  $a_{\text{min}}$  determine the region within which the  $5 \times 10^5$  planets are distributed. In addition, decreasing the minimum contrast increases the range of semi-major axes that are detectable and leads to an increasing number of orbits for which  $f_{\text{obs}} \sim 1.0$  (i.e., orbits that are observable at all times). For  $C_{\text{min}} = 10^{-9}$ , low- to modest-eccentricity orbits with  $f_{\text{obs}} > 1\%$  are confined to  $2 \text{ AU} \lesssim a \lesssim 10 \text{ AU}$ . As we decrease  $C_{\text{min}}$  from left to right in this figure, we see orbits with increasingly larger semi-major axes achieve nonzero  $f_{\text{obs}}$ , reaching  $a \sim 15 \text{ AU}$  and  $a \sim 35 \text{ AU}$  for  $C_{\text{min}} = 5 \times 10^{-10}$  and  $C_{\text{min}} = 10^{-10}$ , respectively.

As mentioned previously, low-inclination orbits are beneficial to direct-imaging observations. In the top left panel, it is particularly clear that orbits with  $f_{\text{obs}} \sim 1.0$  are associated with low inclinations. However, planets with  $i \gtrsim 50^\circ$  can have  $f_{\text{obs}} \sim 15\%$  out to  $a \sim 10 - 30 \text{ AU}$ , depending on  $C_{\text{min}}$ , since phase angles near full phase become observationally accessible. There is also an interesting feature near  $\omega_p \sim 270^\circ$ , which corresponds to orbits with periastron passage occurring at new phase. Near this periastron argument, the region of large  $f_{\text{obs}}$  extends to semi-major axes as large as  $\sim 20 \text{ AU}$  for  $C_{\text{min}} = 10^{-10}$ . For a planet with  $\omega_p \sim 270^\circ$ , the planet/star flux ratio rises with increasing inclination throughout most of its orbit, and the largest angular separations coincide with the highest flux ratios when  $i \gtrsim 50^\circ$  (see Figure 5). These factors collectively increase the semi-major axes for which a planet on such an orbit can have a large observability fraction.

For the remainder of this section, we present the mean observability fraction,  $\langle f_{\text{obs}} \rangle$ , for many MC experiments, which are run under different sets of assumptions. In each case, our goal is to study how the observability fraction depends upon input parameters such as albedo, planetary radius, distance from Earth, minimum achievable contrast, and the semi-major axis distribution. For each experiment, we vary one parameter with respect to a fiducial model, which is comprised of the following assumptions:

- the planetary atmospheres are Rayleigh scattering with  $A_g = 0.5$  (this corresponds to  $\omega \approx 0.95$  for Rayleigh scattering),
- the planets have the radius of Jupiter and orbit stars located 10 pc from Earth,
- the direct-imaging observatory has an OWA =  $1.75''$  and  $C_{\text{min}} = 10^{-9}$  (similar to what is anticipated for WFIRST/AFTA),
- the Keplerian orbital elements are distributed according to the distributions given in Table 2.

Of course, the above assumptions do not fully represent realistic physical/statistical properties of planets or any

future direct-imaging mission. Nevertheless, by varying each parameter of this very simple reference model, it is possible to gain insight into the general problem of directly detecting giant exoplanets in the optical, both in the case of a blind search and observations of stars known to host giant planets.

### 5.1.1. Dependence on Scattering Properties

We start by varying the first of our fiducial model assumptions. Figure 8 shows the dependence of  $\langle f_{\text{obs}} \rangle$  upon the geometric albedo (left panel) and the single-scattering albedo (right panel), assuming Lambert (black), isotropic (red), and Rayleigh (blue) scattering atmospheres. Each curve is composed of many distinct MC experiments, and the three sets of curves in each panel correspond to the indicated IWAs. The WFIRST/AFTA coronagraph is anticipated to have  $\text{IWA} \sim 0.2''$ . Note this value will depend upon the angular separation and wavelength of the observation. For each scattering mechanism, there is a one-to-one correspondence between  $\omega$  and  $A_g$  (see Table 1). Additionally, the phase curves for isotropic and Rayleigh scattering are direct functions of  $\omega$ , and the Lambert phase curve is independent of  $\omega$  (see Figure 1). Thus, given  $A_g$  or  $\omega$ , it is straightforward to calculate the product  $A_g \cdot \Phi(\alpha)$ , which is proportional to the planet/star flux ratio, for an assumed scattering or effective scattering mechanism.

In the left panel of Figure 8, we show the dependence of  $\langle f_{\text{obs}} \rangle$  upon  $A_g$ . For each MC experiment, we assume  $A_g$  and interpolate Table 1 to infer the corresponding  $\omega$ , which is needed to calculate the phase curves for Rayleigh and isotropic scattering. For a given  $A_g$ , the scattering phase functions are entirely responsible for the differences seen between the assumed scattering processes. Note that, since the Lambert phase function is independent of  $\omega$ , the phase function is the same for each black curve. As can be seen in Figure 1, Rayleigh scattering phase curves are systematically lower than isotropic and Lambert phase curves for  $\alpha \lesssim 120^\circ$ . It is for this reason that  $\langle f_{\text{obs}} \rangle$  is always the lowest for Rayleigh scattering. For most  $A_g$ , Rayleigh scattering predicts observability fractions that are  $\sim 20\%$  below the predictions of isotropic and Lambert scattering, regardless of the IWA. At the anticipated IWA for WFIRST/AFTA,  $\langle f_{\text{obs}} \rangle$  decreases sublinearly with  $A_g$  for each scattering process, with maximum and minimum values for Rayleigh scattering of  $\sim 11\%$  for  $A_g = 0.65$  and  $\sim 1\%$  for  $A_g \lesssim 0.1$ . For context, Figure 2 suggests that cool EGPs may have large geometric albedos ( $A_g \sim 0.6 - 0.8$ ) in the optical, particularly for wavelengths  $\lesssim 0.6 \mu\text{m}$  and near the broad water band at  $\sim 0.94 \mu\text{m}$ . As expected, these results suggest planetary geometric albedos can have a dramatic effect on the results of an optical direct-imaging survey.

In the right panel of Figure 8, we show the dependence of  $\langle f_{\text{obs}} \rangle$  upon  $\omega$ . In contrast to the left panel, here we assume  $\omega$  for each MC experiment and use Table 1 to infer the corresponding  $A_g$ . In this case, both  $A_g$  and  $\Phi(\alpha)$  contribute to the differences between the assumed scattering processes. We see that  $\langle f_{\text{obs}} \rangle$  is comparable for Rayleigh and isotropic scattering for all  $\omega$ . This arises from the fact that, for a given  $\omega$ ,  $A_g$  for Rayleigh scattering is systematically *higher* than that for isotropic scattering, whereas  $\Phi(\alpha)$  for Rayleigh scattering is systematically *lower*, leading to roughly consistent observabil-

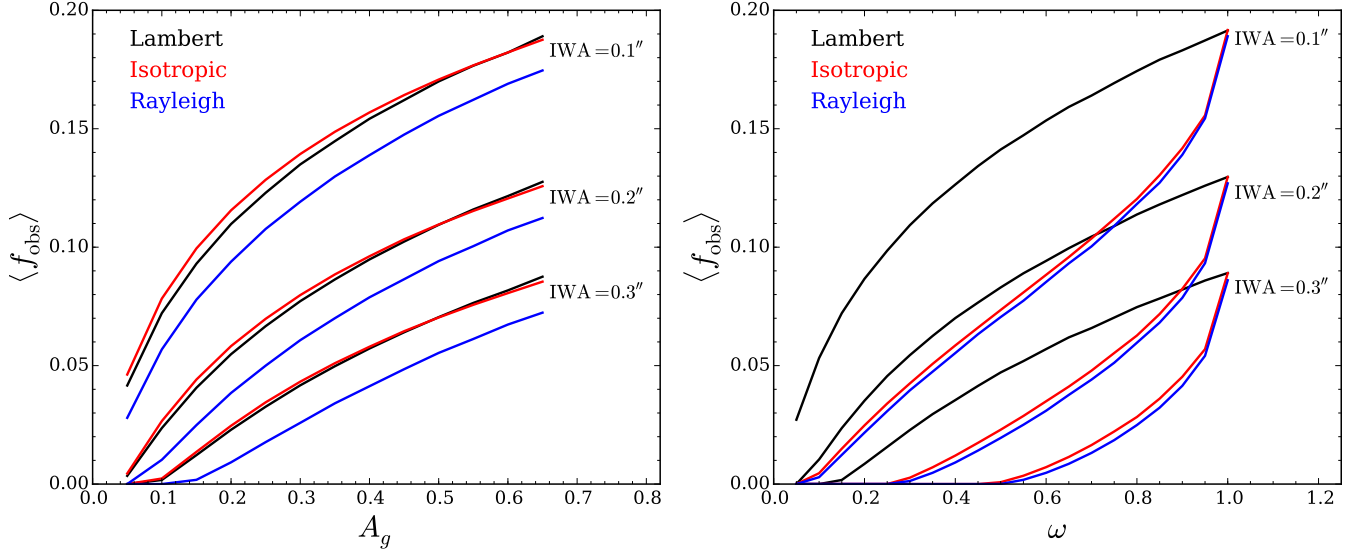


**Figure 8.** The dependence of the mean observability fraction  $\langle f_{\text{obs}} \rangle$  upon the geometric albedo ( $A_g$ , left) and single-scattering albedo ( $\omega$ , right), assuming Lambert (black), isotropic (red), and Rayleigh (blue) scattering atmospheres. In the left panel, we assume  $A_g$  and interpolate Table 1 to infer the corresponding  $\omega$  for each scattering process. In contrast, in the right panel, we assume  $\omega$  and infer  $A_g$  for each scattering process. For each calculation, we assume Jupiter-size planets that orbit stars located 10 pc from Earth, with random orbital parameters drawn from our fiducial distributions (Table 2). The direct-imaging observatory is assumed to have an OWA =  $1.75''$  and  $C_{\text{min}} = 10^{-9}$ . The three sets of curves in both panels correspond to the indicated IWAs. The WFIRST/AFTA coronagraph is anticipated to have IWA =  $0.2''$ .

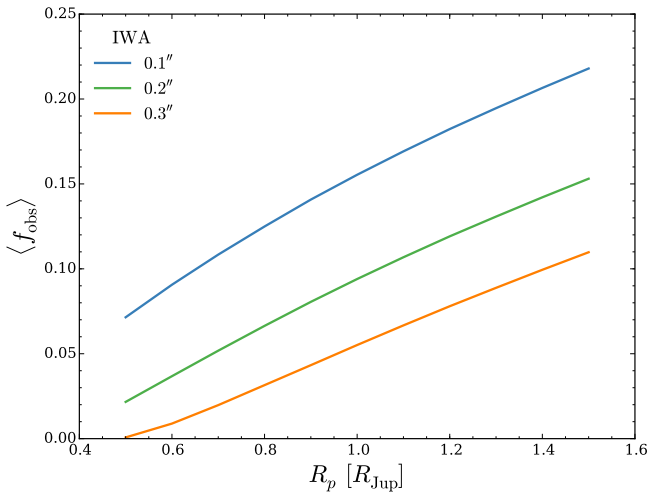


**Figure 9.** Variation of the mean observability fraction  $\langle f_{\text{obs}} \rangle$  with planet radius. With the exception of planet radius, all assumptions are as listed at the end of §5.1. The three curves show  $\langle f_{\text{obs}} \rangle$  for observations made with a coronagraph with the specified IWAs. We note that gas giants are expected to have  $0.8 R_{\text{Jup}} \lesssim R_p \lesssim 1.2 R_{\text{Jup}}$ , but we show a wider range of radii for illustrative purposes.

ity fractions. For conservative scattering ( $\omega = 1.0$ ), the geometric albedos for Lambert, isotropic, and Rayleigh scattering differ by less than  $\sim 13\%$ , and  $\langle f_{\text{obs}} \rangle$  is essentially independent of the assumed scattering mechanism. However, for non-conservative scattering ( $\omega < 1.0$ ), the geometric albedos for isotropic and Rayleigh scattering can be less than those for Lambert scattering by as much as a factor of  $\sim 4$ . As a consequence, Lambert scattering generally predicts significantly higher  $\langle f_{\text{obs}} \rangle$  than both isotropic and Rayleigh scattering.

As a specific example, consider  $\omega = 0.6$ . For this scattering albedo, the Lambert phase function corre-

sponds to a geometric albedo that is a factor of  $\sim 3$  larger than isotropic scattering and a factor of  $\sim 2$  larger than Rayleigh scattering. At the WFIRST/AFTA IWA of  $0.2''$ , this results in  $\langle f_{\text{obs}} \rangle \sim 3\%$  for Rayleigh and isotropic scattering and  $\langle f_{\text{obs}} \rangle \sim 10\%$  for Lambert scattering. Thus, when the geometric albedo is calculated self-consistently with the single-scattering albedo, the assumed scattering phase function can greatly influence the predicted yield from an optical direct-imaging survey. In particular, assuming the Lambert phase function generally results in an overestimate of the detectability of giant planets with respect to the more physically motivated Rayleigh phase function.

### 5.1.2. Dependence on Planet Radius

The planet/star flux ratio is proportional to the square of the planet radius. Therefore, we expect  $\langle f_{\text{obs}} \rangle$  to be sensitive to small variations in planet size, which we have heretofore assumed to be that of Jupiter. Figure 9 shows  $\langle f_{\text{obs}} \rangle$  as a function of planet radius, assuming observations made with a coronagraph that has IWA =  $0.1''$ ,  $0.2''$ , and  $0.3''$ . All assumptions other than planet radius are as listed at the end of §5.1. We note that gas giants are expected to have  $0.8 R_{\text{Jup}} \lesssim R_p \lesssim 1.2 R_{\text{Jup}}$ , but we show a wider range of radii for illustrative purposes. Within the range of expected radii for gas giants, an increase in radius by a factor of  $\sim 1.5$  leads to an increase in  $\langle f_{\text{obs}} \rangle$  by a factor of  $\sim 1.5 - 2.5$ , depending on the IWA. We find that smaller IWAs are less sensitive to variations in planet radius. This effect likely arises from the  $d^{-2}$  dependence of the planet/star flux ratio, which—because of the increasing number of planets at smaller orbital distances that are accessible to smaller IWAs—reduces the weight carried by the  $R_p^2$  dependence of the flux ratio.

### 5.1.3. Dependence on Distance and Minimum Contrast

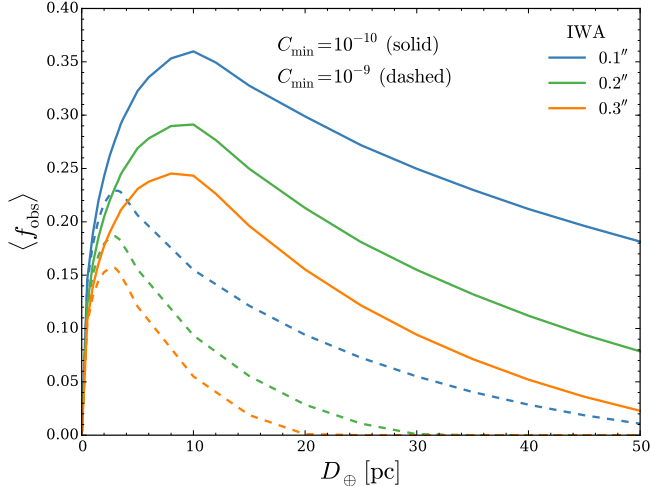


**Figure 10.** The mean observability fraction  $\langle f_{\text{obs}} \rangle$  as a function of distance from Earth ( $D_{\oplus}$ ) and minimum achievable contrast ( $C_{\text{min}}$ ), assuming the IWA =  $0.1''$ ,  $0.2''$ , and  $0.3''$ . Dashed lines assume  $C_{\text{min}} = 10^{-9}$ , and solid lines assume  $C_{\text{min}} = 10^{-10}$ . All other assumptions are as listed at the end of §5.1.

The fiducial model listed at the end of §5.1 assumes direct observations of planet/star systems located a distance  $D_{\oplus} = 10$  pc from Earth with a minimum achievable contrast  $C_{\text{min}} = 10^{-9}$ . It is obvious that the direct detectability of EGPs will vary strongly with both of these parameters. In Figure 10, we investigate this variation in the context of the mean observability fraction. We show  $\langle f_{\text{obs}} \rangle$  for planet/star systems located  $0.01 - 50$  pc from Earth, assuming minimum achievable contrasts of  $10^{-9}$  (dashed lines) and  $10^{-10}$  (solid lines). The calculations assume a coronagraphic instrument with an IWA =  $0.1''$ ,  $0.2''$ , and  $0.3''$ . All other parameters are as listed at the end of §5.1.

WFIRST/AFTA is anticipated to have IWA  $\sim 0.2''$  and  $C_{\text{min}} \sim 10^{-9}$ . In this case, Jupiter-like planets located 10 pc from Earth spend on average  $\sim 10\%$  of their time in observable configurations, whereas the same planets located 30 pc from Earth spend on average  $\sim 0.1\%$  of their time in observable configurations. If instead a minimum contrast of  $10^{-10}$  can be achieved, then these fractions become  $\sim 30\%$  and  $\sim 16\%$ , respectively. At small distances from Earth, we see  $\langle f_{\text{obs}} \rangle$  increases with distance. This trend is the result of planets at sufficiently wide orbital distances to spend some fraction of their orbit outside the OWA, which we have assumed to be  $1.75''$ . Assuming a uniform distribution of stars and IWA =  $0.2''$ , Jupiter-like planets orbiting stars within 10, 30, and 50 pc from Earth have volume-averaged observability fractions of  $\sim 12\%$ ,  $3\%$ , and  $0.5\%$  for  $C_{\text{min}} \sim 10^{-9}$  and  $\sim 28\%$ ,  $20\%$ , and  $13\%$  for  $C_{\text{min}} \sim 10^{-10}$ .

#### 5.1.4. Dependence on the Semi-Major Axis Distribution

Our fiducial model assumes the semi-major axis distribution derived from radial-velocity planets can be extrapolated to wider separations ( $a > 3$  AU). However, the validity of this assumption is highly uncertain, and, as evidenced by Figure 7, the semi-major axis distribution has a large influence on the distribution of observability fractions. In this section, we explore the dependence of  $\langle f_{\text{obs}} \rangle$  upon the semi-major axis distribution

by varying each of its components: the minimum semi-major axis ( $a_{\text{min}}$ ), the maximum semi-major axis ( $a_{\text{max}}$ ), and the power-law index of the distribution ( $\beta$ ).

Our fiducial model assumes  $a_{\text{min}} = 0.03$  AU (note we set  $e = 0$  for any planet with  $a < 0.1$  AU), which has been inferred for radial-velocity planets (Cumming et al. 2008). In Figure 11, we show  $\langle f_{\text{obs}} \rangle$  as a function of  $a_{\text{min}}$ , assuming the indicated IWAs. At a given IWA, the mean observability increases with increasing  $a_{\text{min}}$  until  $a_{\text{min}}/D_{\oplus} \sim \text{IWA}$ , where  $D_{\oplus} = 10$  pc in our fiducial model. Since all of the MC experiments use the same number of planets ( $5 \times 10^5$ ), increasing the minimum semi-major axis forces more planets to exist at larger orbital separations, leading to larger  $\langle f_{\text{obs}} \rangle$  when  $a_{\text{min}}/D_{\oplus} \lesssim \text{IWA}$  and smaller  $\langle f_{\text{obs}} \rangle$  when  $a_{\text{min}}/D_{\oplus} \gtrsim \text{IWA}$ . At the anticipated IWA of WFIRST/AFTA, the mean observability varies by  $\sim 1\%$  for  $a_{\text{min}}$  in the range  $0.03 - 2.0$  AU.

As mentioned in §4.1, recent model-dependent limits on  $a_{\text{max}}$  fall in the range  $\sim 30 - 100$  AU (Brandt et al. 2014). In Figure 12, we test the sensitivity of  $\langle f_{\text{obs}} \rangle$  to a somewhat larger range of  $a_{\text{max}}$ . For a fixed number of planets, smaller  $a_{\text{max}}$  values yield larger  $\langle f_{\text{obs}} \rangle$  values, which is sensible given that more planets will exist at smaller, but still detectable, orbital distances. As  $a_{\text{max}}$  increases,  $\langle f_{\text{obs}} \rangle$  slowly decreases as a result of the increasing number of planets at very large orbital distances, which are too faint to be detected and, in the case of nearly face-on orbits, fall outside the OWA. Over the range  $a_{\text{max}} \sim 30 - 100$  AU,  $\langle f_{\text{obs}} \rangle$  decreases by a factor of  $\sim 1.6$  for each IWA.

The power-law index of the semi-major axis distribution of radial-velocity planets with periods in the range 2–2000 days has been constrained to be  $\beta = -0.61 \pm 0.15$  (Cumming et al. 2008). Our fiducial model assumes this index can be extrapolated to planets at much larger orbital separations. In Figure 13, we test the sensitivity of  $\langle f_{\text{obs}} \rangle$  to variations in the power-law index. As we steepen  $\beta$  towards more negative values, an increasing number of planets begin to pile up at small orbital sep-

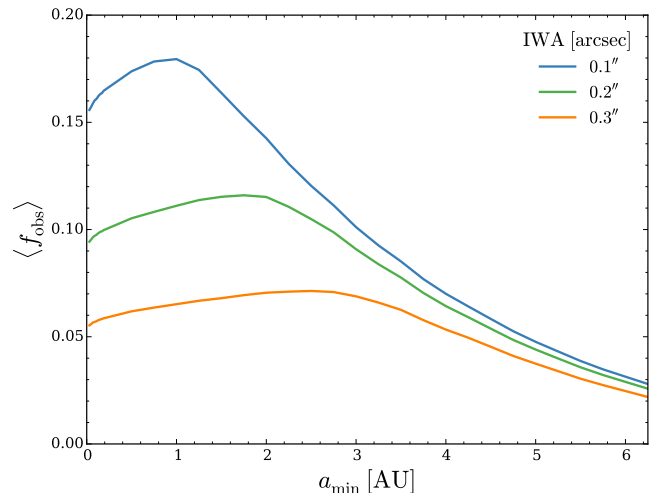


**Figure 11.** Dependence of the mean observability fraction  $\langle f_{\text{obs}} \rangle$  upon the minimum semi-major axis ( $a_{\text{min}}$ ) of the semi-major axis distribution. All other model parameters are as listed at the end of §5.1.

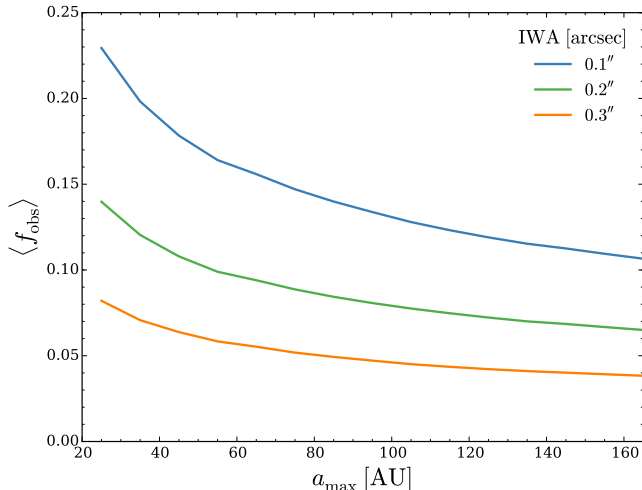


**Figure 12.** Dependence of the mean observability fraction  $\langle f_{\text{obs}} \rangle$  upon the maximum semi-major axis ( $a_{\text{max}}$ ) of the semi-major axis distribution. All other model parameters are as listed at the end of §5.1.

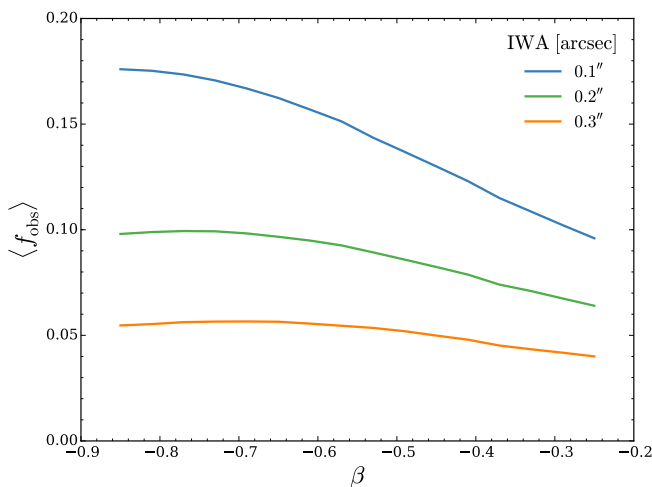


**Figure 13.** Dependence of the mean observability fraction  $\langle f_{\text{obs}} \rangle$  upon the power-law index of the semi-major axis distribution ( $\beta$ ). All other model assumptions are as listed at the end of §5.1.

arations, which leads to larger  $\langle f_{\text{obs}} \rangle$  values. At the anticipated IWA of WFIRST/AFTA,  $\beta = -0.85$  and  $\beta = -0.61$ , which are the estimated indices from Brandt et al. (2014) and Cumming et al. (2008), produce  $\langle f_{\text{obs}} \rangle$  values that are nearly identical. Over the full range of  $\beta$ , the difference between the minimum and maximum  $\langle f_{\text{obs}} \rangle$  values is only  $\sim 3\%$ .

#### 5.1.5. Geometric Albedo as a Function of Distance

Thus far, we have assumed the geometric albedo is constant throughout the orbit of each planet. However, the atmospheric temperature of a planet varies strongly with orbital distance, and such variations determine whether water or ammonia clouds will form. We, therefore, expect the albedo spectrum to vary significantly with orbital distance (Sudarsky et al. 2005). We also expect the albedo spectrum to depend sensitively upon the planet’s mass, age, and parent star. In this section, we compare

our fiducial assumption of  $A_g = 0.5 = \text{constant}$  with two simple models that account for the distance dependence of the albedo spectrum.

The first model is an interpolation of the models shown in Figure 9 of Sudarsky et al. (2005), which depicts the geometric albedo spectra of a Jupiter-mass, 5-Gyr planet orbiting a G2 V star at distances in the range 0.2–15 AU. In Figure 14, we show the predictions of this model for various wavelengths, including wavelengths associated with methane ( $0.74 \mu\text{m}$  and  $0.89 \mu\text{m}$ ), ammonia ( $0.65 \mu\text{m}$ ), and water ( $0.94 \mu\text{m}$ ). We see the geometric albedo, and hence the planet/star flux ratio, is a strong, non-monotonic function of both distance and wavelength.

Using this model for  $A_g$ , we carried out MC experiments for observations at the wavelengths shown in Figure 14, keeping all other parameters as listed at the end of §5.1. For orbital distances  $d > 15$  AU, we set  $A_g$  equal to its value at 15 AU; this does not significantly influence our results, since planets at these separations contribute very little to  $\langle f_{\text{obs}} \rangle$  (see Figure 7). In Figure 15, we show  $\langle f_{\text{obs}} \rangle$  as a function of IWA assuming the “Sudarsky et al.” albedo model (solid lines) and our fiducial assumption of  $A_g = 0.5 = \text{constant}$  (solid black line). As can be seen in the first column of Figure 7, most planets with nonzero  $f_{\text{obs}}$  values have semi-major axes in the range 2 – 10 AU, so it is the variability of  $A_g$  in this region that has the strongest effect on  $\langle f_{\text{obs}} \rangle$ . In the wavelength range we have considered, this model suggests the optimal observability fractions occur for  $\lambda \sim 0.5 - 0.6 \mu\text{m}$ , which Figure 15 indicates is the effective bandpass of our fiducial assumption  $A_g = 0.5$ . At the IWA of WFIRST/AFTA, direct observations in the wavelength range  $\lambda \sim 0.5 - 0.6 \mu\text{m}$  of a Jupiter-like planet located 10 pc from Earth will, on average, be possible for  $\sim 10\%$  of its orbital period. We note that the observed reflected fluxes shortward of  $\sim 0.6 \mu\text{m}$  from Jupiter and Saturn are less than what this model would predict, which is made manifest by the reddish hues of these solar-system planets (Karkoschka 1994; Burrows 2014).

For the second model of the distance dependence of the albedo spectrum, we calculate the equilibrium temperature for each planet as a function of orbital distance in a self-consistent fashion with the albedo spectra. This is accomplished as follows. For each planet in an MC experiment, we assume the planetary atmosphere is homogeneous and Rayleigh scattering. In addition, solar metallicity and a pressure of 0.5 bar are assumed (albedo spectra for such a planet with  $T = 200$  K are shown as black lines in the left column of Figure 2). At a given phase of the planet’s orbit, we assume an initial Bond albedo and calculate the equilibrium temperature. Assuming this to be the temperature of the atmosphere, we generate (scattering, geometric, and spherical) albedo spectra with the methods described in §2.1.2. We then integrate the spherical albedo spectrum to obtain the Bond albedo and calculate a new equilibrium temperature ( $T_{\text{eq}}$ ). We iterate this process until we have achieved self-consistency between the equilibrium temperature and albedo spectra. This procedure is performed at every phase of the planet’s orbit, resulting in a geometric albedo spectrum and phase function that varies with orbital distance. The results of MC experiments assuming this “ $T_{\text{eq}}$  model”



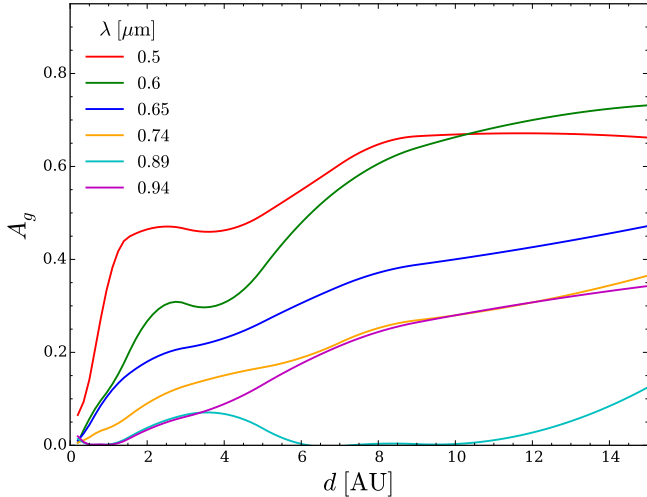


**Figure 14.** The geometric albedo as a function of distance and wavelength for a Jupiter-mass, 5-Gyr planet orbiting a G2 V star. These results are an interpolation of the models shown in Figure 9 of Sudarsky et al. (2005).

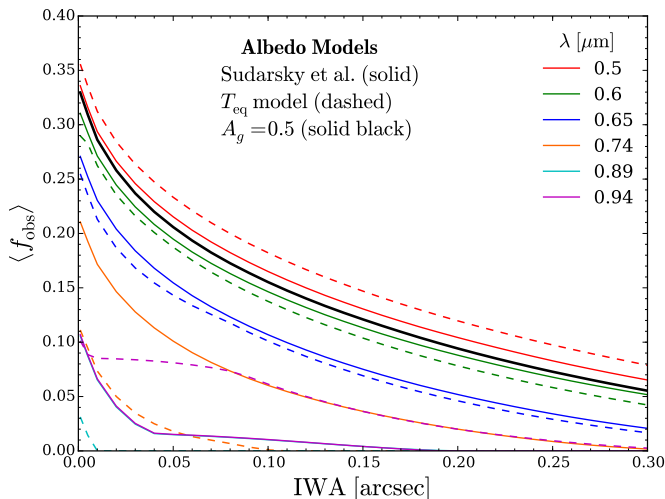


**Figure 15.** Comparison of  $\langle f_{\text{obs}} \rangle$  assuming three models for the albedo spectrum. The “Sudarsky et al.” (solid lines) and “ $T_{\text{eq}}$ ” (dashed lines) models account for the distance dependence of the albedo spectrum, whereas the  $A_g = 0.5$  model (solid black line), which is our fiducial model, holds it constant throughout each planet’s orbit. The solid cyan and purple lines are overlapping, which indicates that orbital distances  $d < 4$  AU are dominating the mean observability at these wavelengths (see Figure 14).

are shown as dashed-lines in Figure 15. We see that this model is roughly consistent with the Sudarsky et al. model for  $\lambda < 0.7 \mu\text{m}$ , but its predictions are very different at longer wavelengths. This model also predicts that the wavelength range  $\lambda \sim 0.5 - 0.6 \mu\text{m}$  offers the optimal observability fractions.

### 5.2. Detection Probabilities

Given assumptions about the orbital parameter distributions and occurrence rates ( $f_p$ ) of a population of planets, the mean observability fractions presented in this work can be translated into the probability that a blind search for such planets will yield a detection. Statistical

studies of planets discovered by the radial-velocity and microlensing methods suggest that the frequency of giant planets with  $a < 20$  AU falls in the range  $f_p \sim 10 - 20\%$  (Cumming et al. 2008; Cassan et al. 2012). If we assume  $f_p = 15\%$ , then calculations based on our fiducial model assumptions, which are listed at the end of §5.1, suggest that the probability of detecting a Jupiter-like planet in a blind search around a star located 10 pc from Earth is  $p = f_p \cdot \langle f_{\text{obs}} \rangle \sim 1.5\%$ , where we have assumed  $\text{IWA} = 0.2''$ . If a minimum contrast of  $10^{-10}$  is assumed, then this probability increases to  $p \sim 4.2\%$ . If the star is located 20 pc from Earth, we find  $p \sim 0.4\%$  for  $C_{\text{min}} = 10^{-9}$  and  $p = 3.2\%$  for  $C_{\text{min}} = 10^{-10}$ . The scaling of  $p$  with parameters such as the IWA, planet radius, distance from Earth, and atmospheric scattering properties can be inferred from the figures presented in this paper. In all but the most optimistic configurations, the probability for detection in a blind search carried out with WFIRST/AFTA’s baseline coronagraphic capabilities is low ( $< 5\%$ ).

By the time direct detection in the optical becomes feasible, long-term radial-velocity campaigns will have likely discovered many wide-separation EGPs, for which a subset of Keplerian elements will be known. Further, it has been estimated that *Gaia* will discover and determine robust orbits for  $\sim 1500$  planets with periods  $\lesssim 6$  yr within 50 pc from Earth (Perryman et al. 2014), including  $\sim 100$  giant planets around known M dwarf host stars within 30 pc (Sozzetti et al. 2014). Direct-imaging surveys that leverage this information can improve their detection probabilities with respect to blind searches, and the tools we have developed for this work can be used to determine both the most promising systems to target and when to observe them. It is important to point out that, as can be inferred from Figures 4–6, the window of time that an EGP is directly detectable can be very brief and sparsely distributed throughout its orbit, suggesting that previous orbital parameter constraints must be very precise if they are to be used to optimize direct-imaging surveys. For a detailed study of the impact of uncertain radial-velocity orbital parameters on direct imaging and spectroscopy of radial-velocity exoplanets, see Brown (2015).

### 5.3. Thermal Emission from Young Planets

Throughout this work, we have focused on cool, relatively old giant planets, for which the flux from thermal emission is negligible compared to the flux from reflected starlight. The thermal emission from a giant planet is age, mass, and metallicity dependent. Furthermore, the particular formation mechanism of giant planets significantly influences the cooling of the planet (e.g., Burrows et al. 1997; Marley et al. 2007; Fortney et al. 2008; Spiegel & Burrows 2012). Regardless of the assumed cooling model, it is reasonable to expect the thermal emission contribution to the optical planet/star flux ratio will increase with planet mass and decrease with planet age.

In Figure 16, we show the planet/star flux ratio (top panel) and associated Rayleigh scattering geometric albedo spectrum (bottom panel) for a representative 7 Jupiter-mass planet orbiting a Sun-like star at an orbital distance of 5 AU, where we have included the effect of blackbody thermal emission from the planet. We use the evolutionary calculations of Burrows et al. (1997) to

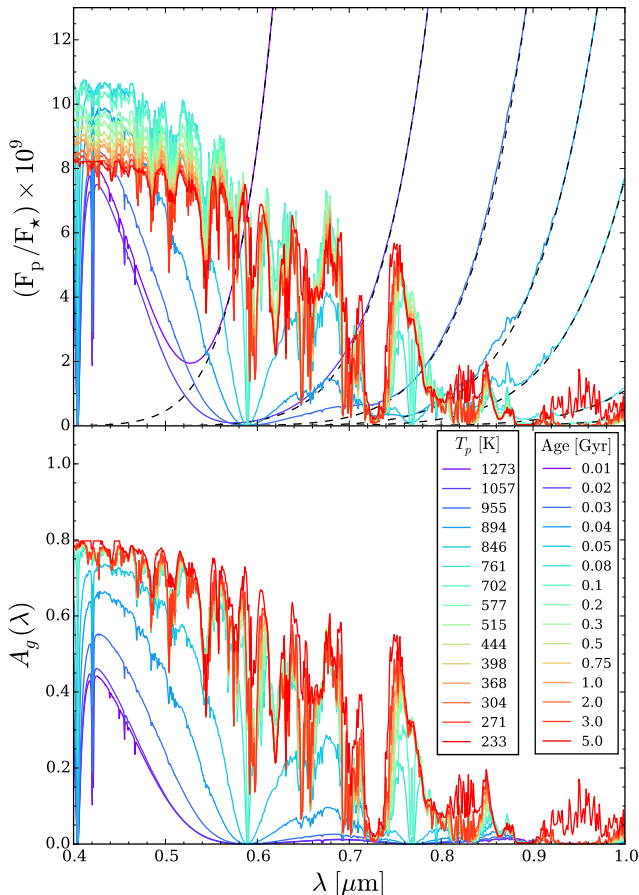


**Figure 16.** The planet/star flux ratio (top) and geometric albedo spectrum (bottom), as a function of wavelength and age, for a 7 Jupiter-mass planet orbiting a Sun-like star at an orbital distance of 5 AU, where we have included the effect of blackbody thermal emission from the planet. The black dashed lines in the top panel show the component of the contrast ratio that is associated with thermal emission from the planet. We use the evolutionary calculations of Burrows et al. (1997) to model the evolution of the age, radius, and temperature of the planet. The atmospheric pressure is 0.5 bar, and solar metallicity is assumed. We have assumed both the star and planet are uniformly luminous blackbodies. The albedo spectrum was calculated with the opacity database from Sharp & Burrows (2007) and the equilibrium chemical abundances from Burrows & Sharp (1999). The atmosphere is assumed to be Rayleigh scattering. The planet age and effective temperature ( $T_p$ ) color-scales apply to both panels.

model the evolution of the age, radius, and temperature of the planet, and the albedo spectrum was calculated with the opacity database from Sharp & Burrows (2007) and equilibrium chemical abundances from Burrows & Sharp (1999). We assume solar metallicity and an atmospheric pressure of 0.5 bar. Both the planet and star are assumed to be uniformly luminous blackbodies. That is, we assume the thermal emission component of the contrast ratio is given by  $R_p^2 B_\lambda(T_p)/R_\star^2 B_\lambda(T_\star)$ , where  $T_p$  is the effective temperature of the planet and  $B_\lambda(T)$  is the Planck function.

In this simple model, the thermal emission from the planet noticeably contributes to the optical planet/star flux ratio only for ages  $< 80$  Myr. Nonetheless, we see it briefly dominates the flux ratio at wavelengths  $\gtrsim 0.5 \mu\text{m}$  when the planet is a mere few tens of millions of years

old, resulting in a planet that transitions from red to blue with increasing age and decreasing effective temperature. The age range over which thermal emission is important will be larger (smaller) for giant planets more (less) massive than 7 Jupiter masses. The decrease in flux at short wavelengths ( $\sim 0.4 - 0.5 \mu\text{m}$ ) for ages  $\gtrsim 100$  Myr is due primarily to the contraction of the planet’s radius, which decreases from  $\sim 1.4 R_{\text{Jup}}$  to  $\sim 1 R_{\text{Jup}}$  throughout its evolution. In contrast, the geometric albedo spectrum is approximately constant over this same wavelength and age interval.

## 6. SUMMARY AND CONCLUSIONS

With the planning of future exoplanet-focused missions such as WFIRST/AFTA well underway, it seems likely that the direct detection of EGPs in the optical will become feasible in the coming decade. Therefore, studies of the observational signatures and direct detectability of reflected light from EGPs are particularly timely and will aid in the design and optimization of these missions. In this work, we have presented an exploration of the direct detectability of EGPs at visible wavelengths, quantified by the fraction of a planet’s orbit for which it is in an observable configuration—its observability fraction  $f_{\text{obs}}$ . Using a suite of Monte Carlo experiments, we investigated the dependence of  $f_{\text{obs}}$  upon various technological and astrophysical parameters such as the inner working angle and minimum achievable contrast of the direct-imaging observatory; the planet’s scattering phase function, geometric albedo, single-scattering albedo, radius, and distance from Earth; and the semi-major axis distribution of EGPs. Unless stated otherwise, we now summarize our results assuming observations of Jupiter-like planets<sup>4</sup>, using an optical coronagraphic instrument with IWA =  $0.2''$  and  $C_{\text{min}} = 10^{-9}$ , which are the baseline design parameters for WFIRST/AFTA.

Low-inclination orbits are highly favorable for direct-imaging observations (Figures 4 and 7). However, planets with  $i \gtrsim 50^\circ$  and  $\omega_p \sim 270^\circ$  (Figures 5 and 7) are generally observable out to larger semi-major axes than planets in other configurations. At a distance of 10 pc from Earth, only (low- to modest-eccentricity) EGPs with semi-major axes in the range  $a \sim 2 - 10$  AU will have  $f_{\text{obs}} > 1\%$ . If  $C_{\text{min}} \sim 10^{-10}$  can be achieved, this range extends out to  $a \sim 35$  AU, with a much larger fraction of orbital parameter space yielding  $f_{\text{obs}} \sim 1$  (Figure 7). Inspection of the bottom row of Figure 7 suggests that the mean direct detectability of EGPs is relatively insensitive to their eccentricity distribution.

The mean observability fraction,  $\langle f_{\text{obs}} \rangle$ , of EGPs is a strong function of their atmospheric scattering properties. For a given geometric albedo, Rayleigh scattering atmospheres predict  $\langle f_{\text{obs}} \rangle$  values that are generally  $\sim 20\%$  below the predictions of isotropic and Lambert scattering atmospheres (left panel, Figure 8). If instead one assumes a single-scattering albedo and self-consistently calculates the phase function for a given scattering mechanism, the often-assumed Lambertian phase function can overestimate the detectability of EGPs by as much as a factor of  $\sim 4$  with respect to the

<sup>4</sup> We remind the reader that we define a “Jupiter-like” planet to be an EGP with the radius of Jupiter,  $A_g = 0.5$ , and a Rayleigh scattering atmosphere.

more physically motivated Rayleigh phase function (right panel, Figure 8).

Within the range of expected radii for gas giants ( $0.8 R_{\text{Jup}} \lesssim R_p \lesssim 1.2 R_{\text{Jup}}$ ), an increase in radius by a factor of  $\sim 1.5$  leads to an increase in  $\langle f_{\text{obs}} \rangle$  by a factor of  $\sim 1.8$  (Figure 9). We find that smaller IWAs are less sensitive to variations in planet radius. This effect likely arises from the  $d^{-2}$  dependence of the planet/star flux ratio, which—because of the increasing number of planets at smaller separations that are accessible to smaller IWAs—reduces the weight carried by the  $R_p^2$  dependence of the flux ratio.

An EGP located 10 pc from Earth will spend on average  $\sim 10\%$  of its time in observable configurations, whereas the same planet located 30 pc from Earth will spend on average  $\sim 0.1\%$  of its time in observable configurations. If a minimum contrast of  $10^{-10}$  can be achieved, then these fractions become  $\sim 30\%$  and  $\sim 16\%$ , respectively (Figure 10). Assuming a uniform distribution of stars, EGPs orbiting stars within 10, 30, and 50 pc from Earth have volume-averaged observability fractions of  $\sim 12\%$ ,  $3\%$ , and  $0.5\%$  for  $C_{\text{min}} \sim 10^{-9}$  and  $\sim 28\%$ ,  $20\%$ , and  $13\%$  for  $C_{\text{min}} \sim 10^{-10}$ . Thus, the scientific return from a future optical direct-imaging survey will depend critically upon its minimum achievable contrast, as well as the number of wide-separation EGPs that exist within a few tens of parsecs from Earth.

In §5.1.4 we explored the dependence of  $\langle f_{\text{obs}} \rangle$  upon the semi-major axis distribution of EGPs by varying each of its components: the minimum semi-major axis ( $a_{\text{min}}$ ), the maximum semi-major axis ( $a_{\text{max}}$ ), and the power-law index of the distribution ( $\beta$ ). Given constraints from radial-velocity planets and infrared direct-imaging surveys, the uncertainty in  $\langle f_{\text{obs}} \rangle$  is dominated by the uncertainty in  $a_{\text{max}}$ . For  $a_{\text{max}}$  in the range 30 – 100 AU, which is the model-dependent limit set by Brandt et al. (2014),  $\langle f_{\text{obs}} \rangle$  varies by a factor of  $\sim 1.6$  (Figure 12).

The albedo spectrum of a giant planet is expected to be a non-monotonic function of both distance and wavelength (Figure 15 and Sudarsky et al. 2005). Using two simple models for the distance- and wavelength-dependence of the geometric albedo, we find that bluer wavelengths result in larger  $\langle f_{\text{obs}} \rangle$  values, which is to be expected given that we are interested in reflected-light observations. We caution that, as revealed by their reddish hues, the observed reflected fluxes shortward of  $\sim 0.6 \mu\text{m}$  from Jupiter and Saturn are less than what our models would predict.

As described in §5.2, the mean observability fraction for a population of planets is proportional to the probability ( $p$ ) that a blind search for such planets will yield a detection:  $p = f_p \cdot \langle f_{\text{obs}} \rangle$ , where  $f_p$  is the planet occurrence rate. The scaling of  $p$  with parameters such as IWA,  $C_{\text{min}}$ , planet radius, distance from Earth, and atmospheric scattering properties can be inferred from the figures presented in this paper. In all but the most optimistic configurations, the probability for detection in a blind search carried out with WFIRST/AFITA’s baseline coronagraphic capabilities is low ( $< 5\%$ ).

Finally, we note that thermal emission from young EGPs can provide a non-negligible contribution to optical planet/star flux ratios. Assuming the evolutionary calculations of Burrows et al. (1997), the thermal emis-

sion from a 7 Jupiter-mass planet orbiting a Sun-like star briefly dominates the flux ratio at wavelengths  $\gtrsim 0.5 \mu\text{m}$  when the planet is a few tens of millions of years old, becoming completely negligible after  $\sim 80$  Myr. The result is a planet that transitions from red to blue with increasing age and decreasing effective temperature (Figure 16). The age range over which the thermal emission contribution to the optical flux ratio is significant will be larger (smaller) for giant planets more (less) massive than the representative 7 Jupiter-mass planet we have considered here.

JPG is supported by the National Science Foundation Graduate Research Fellowship under Grant No. DGE 1148900. A.B. would like to acknowledge support in part under NASA grant NNX15AE19G, JPL subcontract no. 1513640, NASA HST awards HST-GO-13467.10-A, HST-GO-12550.02, and HST-GO-12473.06-A, and JPL/Spitzer contracts 1439064 and 1477493.

#### REFERENCES

- Barman, T. S., Macintosh, B., Konopacky, Q. M., & Marois, C. 2011, *ApJ*, 733, 65
- Batalha, N. M., Rowe, J. F., Bryson, S. T., et al. 2013, *ApJS*, 204, 24
- Beichman, C. A., Krist, J., Trauger, J. T., et al. 2010, *PASP*, 122, 162
- Beuzit, J.-L., Feldt, M., Dohlen, K., et al. 2008, in *Society of Photo-Optical Instrumentation Engineers (SPIE) Conference Series*, Vol. 7014, *Society of Photo-Optical Instrumentation Engineers (SPIE) Conference Series*, 18
- Brandt, T. D., McElwain, M. W., Turner, E. L., et al. 2014, *ApJ*, 794, 159
- Brown, R. A. 2015, *ApJ*, 805, 188
- Buenzli, E., & Schmid, H. M. 2009, *A&A*, 504, 259
- Burrows, A. 2014, *ArXiv e-prints*, arXiv:1412.6097
- Burrows, A., & Sharp, C. M. 1999, *ApJ*, 512, 843
- Burrows, A., Sudarsky, D., & Hubeny, I. 2004, *ApJ*, 609, 407
- Burrows, A., Marley, M., Hubbard, W. B., et al. 1997, *ApJ*, 491, 856
- Cahoy, K. L., Marley, M. S., & Fortney, J. J. 2010, *ApJ*, 724, 189
- Cassan, A., Kubas, D., Beaulieu, J.-P., et al. 2012, *Nature*, 481, 167
- Chauvin, G., Lagrange, A.-M., Dumas, C., et al. 2004, *A&A*, 425, L29
- Chauvin, G., Lagrange, A.-M., Zuckerman, B., et al. 2005, *A&A*, 438, L29
- Cumming, A., Butler, R. P., Marcy, G. W., et al. 2008, *PASP*, 120, 531
- Deming, D., Seager, S., Winn, J., et al. 2009, *PASP*, 121, 952
- Dyudina, U. A., Sackett, P. D., Bayliss, D. D. R., et al. 2005, *ApJ*, 618, 973
- Fortney, J. J., Marley, M. S., Saumon, D., & Lodders, K. 2008, *ApJ*, 683, 1104
- Fressin, F., Torres, G., Charbonneau, D., et al. 2013, *ApJ*, 766, 81
- Hansen, J. E., & Hovenier, J. W. 1974, in *IAU Symposium*, Vol. 65, *Exploration of the Planetary System*, ed. A. Woszczyk & C. Iwaniszewska, 197–200
- Howard, A. W., Marcy, G. W., Johnson, J. A., et al. 2010, *Science*, 330, 653
- Hu, R. 2014, *ArXiv e-prints*, arXiv:1412.7582
- Irwin, P. G. J., Calcutt, S. B., Weir, A. L., Taylor, F. W., & Carlson, R. W. 2002, *Advances in Space Research*, 29, 285
- Janson, M. 2010, *MNRAS*, 408, 514
- Kane, S. R. 2013, *ApJ*, 766, 10
- Kane, S. R., & Gelino, D. M. 2010, *ApJ*, 724, 818
- . 2011, *ApJ*, 729, 74
- Karkoschka, E. 1994, *Icarus*, 111, 174
- Karkoschka, E., & Tomasko, M. G. 2011, *Icarus*, 211, 780
- Kipping, D. M. 2013, *MNRAS*, 434, L51
- Kuzuhara, M., Tamura, M., Kudo, T., et al. 2013, *ApJ*, 774, 11

- Lagrange, A.-M., Gratadour, D., Chauvin, G., et al. 2009, *A&A*, 493, L21
- Macintosh, B. A., Graham, J. R., Palmer, D. W., et al. 2008, in *Society of Photo-Optical Instrumentation Engineers (SPIE) Conference Series*, Vol. 7015, Society of Photo-Optical Instrumentation Engineers (SPIE) Conference Series, 18
- Madhusudhan, N., & Burrows, A. 2012, *ApJ*, 747, 25
- Marley, M., Lupu, R., Lewis, N., et al. 2014, *ArXiv e-prints*, arXiv:1412.8440
- Marley, M. S., Fortney, J. J., Hubickyj, O., Bodenheimer, P., & Lissauer, J. J. 2007, *ApJ*, 655, 541
- Marley, M. S., Gelino, C., Stephens, D., Lunine, J. I., & Freedman, R. 1999, *ApJ*, 513, 879
- Marois, C., Macintosh, B., Barman, T., et al. 2008, *Science*, 322, 1348
- Marois, C., Zuckerman, B., Konopacky, Q. M., Macintosh, B., & Barman, T. 2010, *Nature*, 468, 1080
- Neuhäuser, R., Guenther, E. W., Wuchterl, G., et al. 2005, *A&A*, 435, L13
- Nielsen, E. L., & Close, L. M. 2010, *ApJ*, 717, 878
- Oppenheimer, B. R., & Hinkley, S. 2009, *ARA&A*, 47, 253
- Perryman, M., Hartman, J., Bakos, G. A., & Lindgren, L. 2014, *ApJ*, 797, 14
- Satoh, T., Itoh, S., Kawabata, K., Tenma, T., & Akabane, T. 2000, *PASJ*, 52, 363
- Seager, S., Whitney, B. A., & Sasselov, D. D. 2000, *ApJ*, 540, 504
- Sharp, C. M., & Burrows, A. 2007, *ApJS*, 168, 140
- Skrutskie, M. F., Jones, T., Hinz, P., et al. 2010, in *Society of Photo-Optical Instrumentation Engineers (SPIE) Conference Series*, Vol. 7735, Society of Photo-Optical Instrumentation Engineers (SPIE) Conference Series, 3
- Sozzetti, A., Giacobbe, P., Lattanzi, M. G., et al. 2014, *MNRAS*, 437, 497
- Spergel, D., Gehrels, N., Baltay, C., et al. 2015, *ArXiv e-prints*, arXiv:1503.03757
- Spiegel, D. S., & Burrows, A. 2012, *ApJ*, 745, 174
- Stam, D. M., Hovenier, J. W., & Waters, L. B. F. M. 2004, *A&A*, 428, 663
- Sudarsky, D., Burrows, A., & Hubeny, I. 2003, *ApJ*, 588, 1121
- Sudarsky, D., Burrows, A., Hubeny, I., & Li, A. 2005, *ApJ*, 627, 520
- Sudarsky, D., Burrows, A., & Pinto, P. 2000, *ApJ*, 538, 885
- Suzuki, R., Kudo, T., Hashimoto, J., et al. 2010, in *Society of Photo-Optical Instrumentation Engineers (SPIE) Conference Series*, Vol. 7735, Society of Photo-Optical Instrumentation Engineers (SPIE) Conference Series, 30
- Traub, W. A., & Oppenheimer, B. R. 2010, *Direct Imaging of Exoplanets*, ed. S. Seager, 111–156

## APPENDIX

The orbital phase angle ( $\alpha$ ) is related to the true anomaly ( $\theta$ ) and the Keplerian elements by<sup>5</sup>

$$\begin{aligned} \cos \alpha &= \sin(\theta + \omega_p) \sin i \sin \Omega - \cos \Omega \cos(\theta + \omega_p), \\ &= \sin(\theta + \omega_p) \sin i, \end{aligned} \quad (\text{A.1})$$

where  $i$  is the orbital inclination,  $\omega_p$  is the argument of periastron, and  $\Omega$  is the longitude of the ascending node. The second equality in Equation (A.1) comes from the assumption that  $\Omega = 90^\circ$ . For the orbit orientation, we use the convention  $\alpha = \theta = 0^\circ$  when  $\omega_p = i = 90^\circ$ . The range of observable phase angles depends only on the inclination of the orbit:  $90^\circ - i < \alpha < 90^\circ + i$ . For eccentric orbits, the light curve will vary even when  $i = 0^\circ$ . This is due to changes in the orbital distance ( $d$ ) along the orbit, which is given by

$$d = \frac{a(1 - e^2)}{1 + e \cos \theta}. \quad (\text{A.2})$$

The Keplerian elements are connected to time ( $t$ ) through the mean anomaly ( $M = 2\pi(t - t_p)/P$ , where  $t_p$  is the time of periastron passage), which is related to the eccentric anomaly ( $E$ ) by Kepler's equation:

$$M = E - e \sin E. \quad (\text{A.3})$$

$E$  can be expressed in terms of the true anomaly as

$$\sin E = \frac{\sin \theta \sqrt{1 - e^2}}{1 + e \cos \theta}. \quad (\text{A.4})$$

We can then relate the planet's true anomaly to time:

$$\begin{aligned} \frac{t - t_p}{P} &= \frac{1}{2\pi} \left[ -\frac{e \sin \theta \sqrt{1 - e^2}}{1 + e \cos \theta} \right. \\ &\quad \left. + 2 \tan^{-1} \left( \sqrt{\frac{1 - e}{1 + e}} \tan \frac{\theta}{2} \right) \right]. \end{aligned} \quad (\text{A.5})$$

Thus, for an arbitrary orbit orientation, Equations (A.1) and (A.5) combine to yield the exact orbital phase at any time.

<sup>5</sup> Note  $\Omega$  is necessary when an absolute celestial frame is designated. However, one can assume  $\Omega = 90^\circ$  or simply ignore this

parameter when the system itself is allowed to provide a natural orientation.